A&A, 694, A171 (2025)
https://doi.org/10.1051/0004-6361/202451290

Astronomy & Astrophysics

The host galaxies of radio-loud quasars at $z > 5$ with ALMA

C. Mazzucchelli[1,⋆], R. Decarli[2], S. Belladitta[2,3], E. Bañados[3], R. A. Meyer[4], T. Connor[5], E. Momjian[6], S. Rojas-Ruiz[7], A.-C. Eilers[8], Y. Khusanova[3], E. P. Farina[9], A. B. Drake[10], F. Walter[3], F. Wang[11], M. Onoue[12,13,14], and B. P. Venemans[15]

[1] Instituto de Estudios Astrofísicos, Facultad de Ingeniería y Ciencias, Universidad Diego Portales, Avenida Ejercito Libertador 441, Santiago, Chile
[2] INAF – Osservatorio di Astrofisica e Scienza dello Spazio di Bologna, Via Gobetti 93/3, I-40129 Bologna, Italy
[3] Max Planck Institut für Astronomie, Königstuhl 17, D-69117 Heidelberg, Germany
[4] Department of Astronomy, University of Geneva, Chemin Pegasi 51, 1290 Versoix, Switzerland
[5] Center for Astrophysics | Harvard & Smithsonian, 60 Garden St., Cambridge, MA 02138, USA
[6] National Radio Astronomy Observatory, P.O. Box O, 1011 Lopezville Road, Socorro, NM 87801, USA
[7] Department of Physics and Astronomy, University of California, Los Angeles, 430 Portola Plaza, Los Angeles, CA 90095, USA
[8] MIT Kavli Institute for Astrophysics and Space Research, 77 Massachusetts Ave., Cambridge, MA 02139, USA
[9] Gemini Observatory, NSF's NOIRLab, 670 N A'ohoku Place, Hilo, Hawai'i 96720, USA
[10] Centre for Astrophysics Research, University of Hertfordshire, Hatfield, Hertfordshire AL10 9AB, UK
[11] Steward Observatory, University of Arizona, 933 N Cherry Avenue, Tucson, AZ 85721, USA
[12] Kavli Institute for the Physics and Mathematics of the Universe (Kavli IPMU, WPI), The University of Tokyo Institutes for Advanced Study, The University of Tokyo, Kashiwa, Chiba 277-8583, Japan
[13] Center for Data-Driven Discovery, Kavli IPMU (WPI), UTIAS, The University of Tokyo, Kashiwa, Chiba 277-8583, Japan
[14] Kavli Institute for Astronomy and Astrophysics, Peking University, Beijing 100871, China
[15] Leiden Observatory, Leiden University, PO Box 9513, 2300 RA Leiden, The Netherlands

Received 28 June 2024 / Accepted 14 November 2024

ABSTRACT

The interaction between radio jets and quasar host galaxies plays a paramount role in quasar and galaxy co-evolution. However, very little is known at present about this interaction at very high−z. Here, we present new Atacama Large Millimeter/submillimeter Array (ALMA) observations in Bands 7 and 3 of six radio-loud (RL) quasar host galaxies at $z > 5$. We recovered [C II] 158 µm line and underlying dust continuum emission at $>2\sigma$ for five sources, while we obtained upper limits for the CO(6-5) emission line and continuum for the remaining source. At the spatial resolution of our observations (∼1″.0–1″.4), we did not recover any perturbed or extended morphologies or kinematics, which are known signatures of potential mergers. These galaxies already host large quantities of gas ($\sim 10^{10}\,M_\odot$), with [C II] luminosities of $L_{[\rm C\,II]} \sim 10^{8-9}\,L_\odot$ and [C II]-based star formation rates of 30−400 $M_\odot\,{\rm yr}^{-1}$. In building their radio/submillimeter (radio/submm) spectral energy distributions (SEDs), we found that in at least four cases, the 1 mm continuum intensity arises from a combination of synchrotron and dust emission. The initial estimation of synchrotron contribution at 300 GHz in these cases is of ≳10%. Assuming a scenario where the continuum emission is solely due to cold dust as an upper limit, we obtained infrared (IR) luminosities of $L_{\rm IR} \sim 10^{11-12}\,L_\odot$. We compared the properties of the sources inspected here with a large collection of radio-quiet sources from the literature, as well as a sample of RL quasars from previous studies at comparable redshifts. We recovered a mild potential decrease in $L_{[\rm C\,II]}$ for the RL sources, which might be due to a suppression of the cool gas emission due to the radio jets. We did not find any [C II] emitting companion galaxy candidate around the five RL quasars observed in Band 7. Given the depth of our dataset, this result is still consistent with what has been observed around radio-quiet quasars. Future higher spatial-resolution observations, over a broader frequency range, of high−z RL quasars hosts will allow us to further improve our understanding of the physics of these sources.

Key words. ISM: general – galaxies: high-redshift – quasars: general – early Universe – dark ages, reionization, first stars

1. Introduction

Quasars are among the most luminous, non-transient sources in the Universe. They can be observed at very large distances, hence, at large look-back times. Over the last two decades, the number of quasars known at high redshift ($z \gtrsim 5$, i.e., within one Gyr since the Big Bang) increased dramatically, with more than 400 sources discovered thus far (e.g., Fan et al. 2001, 2006, Bañados et al. 2016, Mazzucchelli et al. 2017, Matsuoka et al. 2018, Reed et al. 2019, Yang et al. 2019a, 2023, Wenzl et al. 2021) up to $z \sim 7.5$ (Bañados et al. 2018a, Yang et al. 2020, Wang et al. 2021; also see Fan et al. 2023 for a recent review). Very large supermassive black holes (SMBH) have been observed in their centers ($>10^8\,M_\odot$; e.g., Willott et al. 2015, Yang et al. 2021, Farina et al. 2022, Mazzucchelli et al. 2023), surrounded by gas already enriched at (super)solar metallicities (e.g., Xu et al. 2018, Onoue et al. 2020, Lai et al. 2022).

Observations of the stellar radiation from the host galaxies of high-redshift quasars have been challenging (e.g., Decarli et al. 2012, Mechtley et al. 2012, Marshall et al. 2020) due to the overwhelming radiation from the nuclear engine. It was only very recently that observations with the *James Webb* Space Telescope

⋆ Corresponding author; chiara.mazzucchelli@mail.udp.cl

(JWST) were able to uncover such stellar emission in a few sources (e.g., Ding et al. 2023, Marshall et al. 2023, Stone et al. 2023, 2024, Yue et al. 2024, Onoue et al. 2024). Conversely, the properties of the host galaxies can be more easily explored with observations of the cool gas and dust emission from the interstellar medium (ISM), recovered in the (sub)mm regime at high−z. In particular, the [C II] 158 µm emission line is the main coolant of the ISM, and can emit up to 3% of the total galactic output (e.g., Carilli & Walter 2013). Initial studies of a few massive sources known at that time were pursed with the IRAM Plateau de Bure interferometer in the 2010 s (e.g., Maiolino et al. 2005, Walter et al. 2009, Wang et al. 2010). Afterwards, the advent of the Atacama Large Millimeter/submillimeter Array (ALMA) paved the way for the exploration of large, statistically significant samples of quasars (e.g., Wang et al. 2013, 2024a, Willott et al. 2015, 2017, Trakhtenbrot et al. 2017, Decarli et al. 2018, Venemans et al. 2018, 2020, Izumi et al. 2018, 2019, 2021, Nguyen et al. 2020). So far, the host galaxies of almost 80 quasars have been observed in the (sub)millimeter at $z > 5$. The main results of these observations are as follows: *a*) quasar hosts already contain large reservoirs of gas and dust ($M_{\rm dust} > 10^8\,M_\odot$) and are very rapidly forming stars, with a star formation rate (SFR) up to >100−1000 $M_\odot\,{\rm yr}^{-1}$; *b*) the central SMBHs seem to be overmassive with respect to predictions from the SMBH-host galaxy mass relation observed in the Local Universe (e.g.; Venemans et al. 2016, Pensabene et al. 2020, Neeleman et al. 2021), although this discrepancy seems less marked at lower luminosities and black hole masses (e.g., Izumi et al. 2021); *c*) quasar hosts present a variety of kinematics, such as rotation-supported, dispersion-dominated, or disturbed by close companions and/or mergers events (e.g., Neeleman et al. 2021) – whereas observational studies provide mixed results for the presence of major molecular and/or cool gas outflows (e.g., Decarli et al. 2018, Bischetti et al. 2019, Novak et al. 2020, Meyer et al. 2022a); and, finally, *d*) ≳20−40% of these sources are surrounded by overdensities of galaxies on scales of tens of kpc (e.g., Decarli et al. 2017, Trakhtenbrot et al. 2017, Nguyen et al. 2020, Venemans et al. 2020), which are extremely dust- and gas-rich and severely obscured (e.g., Mazzucchelli et al. 2019). The large sample of high-redshift quasars now observed in the submillimeter (submm) is dominated by radio-quiet (RQ) quasars due to the absence of dedicated ALMA follow-up for the radio-loud (RL) population.

A fraction of quasars (i.e., ∼10−20%) irrespective of redshift up to $z \gtrsim 6$, namely, within the Epoch of Reionization (EOR, e.g., Bañados et al. 2015a, Liu et al. 2021; but see also Sbarrato et al. 2022) do indeed show strong radio emission, associated with powerful jets. These sources are defined as RL quasars; namely, they are characterized by a radio loudness parameter of $R_{4400} = f_{\nu,5\,{\rm GHz}}/f_{4400\,\text{Å}} > 10$ (Kellermann et al. 1989) or $R_{2500} = f_{\nu,5\,{\rm GHz}}/f_{2500\,\text{Å}} > 10$ (Jiang et al. 2007), where $f_{\nu,5\,{\rm GHz}}$, $f_{4400\,\text{Å}}$, and $f_{2500\,\text{Å}}$ are the flux densities at 5 GHz, 4400 Å and 2500 Å, respectively. These two quantities provide similar results for an unobscured type-1 quasar. In this paper, we consider R_{2500} as our radio loudness parameter. Radio jets are thought to be key elements in the host galaxy-SMBH (co)evolution, via so-called radio-mode feedback. Indeed, on the one hand, jets can reduce star formation by sweeping away the gas reservoir (e.g., Villar Martín et al. 2014); whereas on the other hand, they might enhance the formation of new stars, especially at high−z. This type of star formation happens via shock-induced gravitational collapse of gas clouds in an in-homogeneous and dense medium (e.g., Silk 2013, Salomé et al. 2015, Fragile et al. 2017). Moreover, RL quasars are routinely observed in rich galactic environments (e.g., Wylezalek et al. 2013, Venemans et al. 2007) and are considered to be optimal targets for uncovering overdensities of galaxies in the EOR (e.g., Zheng et al. 2006, Ajiki et al. 2006, Bosman et al. 2020). Currently, there are 50 RL quasars known at $z \gtrsim 5$ (see Bañados et al. 2021 and references there-in), out of which 5 are classified as blazars (i.e., with the relativistic jets aligned with our line of sight; e.g., Belladitta et al. 2019, 2020, Banados et al. 2024a). More than half of these sources have been identified in the last two years (e.g., Gloudemans et al. 2022, Bañados et al. 2023, Belladitta et al. 2023). However, very few of their host galaxies have been studied so far. Rojas-Ruiz et al. (2021) observed the $z \sim 5.8$ RL quasar PSO352-15 with a collection of (sub)mm and radio data, obtained with ALMA, NOrthern Extended Millimeter Array (NOEMA), and the upgraded Giant Metrewave Radio Telescope (uGMRT). They found that the total submm emission cannot be uniquely explained by dust emission and that synchrotron radiation contributes down to these frequencies. Khusanova et al. (2022) observed four other $z > 6$ RL quasars in the Northern Hemisphere with NOEMA, targeting their dust and [C II] emission lines. While the host of the highest reshift ($z \sim 6.8$) RL quasar known so far has not been detected, some of the remaining hosts show asymmetric line profiles (indicative of a potential merger or strong outflow) and SFRs comparable to RQ quasars hosts. Very recently, Banados et al. (2024a) discovered a blazar at $z \sim 7$ and Banados et al. (2024b) reported NOEMA (2021) and ALMA (2022) observations of this source. They recovered a large (>30%) flux variation within only ten months and they estimated a synchrotron contribution to the observed ∼230 GHz flux as high as ∼80%.

Here, we present new ALMA observations of the dust continuum and [C II] or CO(6-5) emission lines of the host galaxies of six $5 < z < 6$ RL quasars and one RQ source[1]. This paper is organized as follows. In Sect. 2, we report our sample and observations. In Sect. 3, we describe our methods to derive continuum and emission lines measurements. In Sect. 4, we report our redshift estimates, present the radio-mm spectral energy distributions (SEDs) of our RL quasars, calculate gas and [C II] luminosities, SFRs, dust, dynamical, and molecular gas masses, and place them in the context of RQ quasars host galaxies' observations drawn from the literature. We also compare the infrared (host galaxies) and UV (nuclear emission) properties, and we search for the presence of further line emitting galaxies in their fields. Finally, we discuss our results in Sect. 5 and present our conclusions in Sect. 6.

Throughout this work, we use a cosmology with $H_0 = 67.8\,{\rm km\,s{-}1\,Mpc^{-1}}$, $\Omega_M = 0.3$, and $\Omega_\Lambda = 0.7$. The age of the Universe at $z = 5.5$ is 1.04 Gyr and the transverse physical scale is 6.1 kpc per arcsec. All magnitudes are reported in the AB system.

2. Sample and observations

For this study, we focus on high-redshift ($z > 5$) RL quasars, observable from ALMA (Declination <20 deg). At the time of the submission of the proposal (April 2018), the source J2053+0047 was tentatively classified as RL by Bañados et al. (2015b), based on data from the Faint Images of the Radio Sky at Twenty cm survey (FIRST, Becker et al. 1995), with a radio loudness parameter of $R_{4400} = 44.1 \pm 18.7$. However, Liu et al.

[1] At the time of observations, J2053+0047 was misclassified as RL; see Sect. 2 for more details.

Table 1. Sample of quasars in this study.

Name	RA (J2000)	Dec (J2000)	z	z method	M_{1450}	R_{2500}	Reference Disc / z / M_{1450}
J0131-0321 (†)	01:31:27.3400	−03:21:00.180	5.1904 ± 0.0003	Mg II	−29.11	116 ± 9	1 / 2 / 1
PSO055-00	03:41:41.8580	−00:48:12.740	5.68 ± 0.05	template	−26.37	83 ± 9	3 / 3 / 4
PSO135+16	09:01:32.6530	16:15:06.830	5.63 ± 0.05	template	−25.91	177 ± 18	3 / 3 / 4
J1034+2033	10:34:18.6500	20:33:00.220	5.01 ± 0.02	z_VI (‡)	−27.76	47 ± 4	5 / 6 / 7
J2228+0110	22:28:43.5350	01:10:32.200	5.903 ± 0.0002	Lyα	−24.50	71 ± 15	8 / 9 / 8
PSO352–15	23:29:36.8362	−15:20:14.460	5.84 ± 0.02	template	−25.60	1470 ± 110	10 / 10 / 10
J2053+0047 (⋆)	20:53:21.766	+00:47:06.80	5.92 ± 0.03	Lyα	−25.30	<9.7 (∓)	11 / 11 / 11

Notes. The radio-loudness parameter is from Bañados et al. (2021; and references therein), with the exception of POS352-15, where R_{2500} is from Rojas-Ruiz et al. (2021). Further references are: 1) Yi et al. (2014); 2) this work; 3) Bañados et al. (2015b); 4) Bañados et al. (2016); 5) Schneider et al. (2010); 6) Pâris et al. (2018); 7) Bañados et al. (2021); 8) Zeimann et al. (2011); 9) Roche et al. (2014); 10) Bañados et al. (2018b); 11) Jiang et al. (2009). (†)Classified as blazar (see Section 2 for details). (‡)See Pâris et al. (2018) for a discussion on different redshift estimates. (⋆)We note J2053+0047 was reclassified as a RQ quasar with deeper radio VLA observations (see Section 2 for details). (∓)Limit on radio-loudness parameter is obtained from Liu et al. (2021).

(2021) showed it to be RQ, based on deeper follow-up data with the Karl G. Jansky Very Large Array (VLA), with $R_{4400} < 9.7$. We still provide our measurements and results for this quasar in the paper, but we label this object as RQ. We list in Table 1 the general properties of our sample, namely: the coordinates, literature redshifts, magnitude at rest-frame 1450 Å, and the radio loudness parameter.

ALMA Cycle 7 observations (program ID: 2019.1.00840.S, PI: Mazzucchelli) were obtained between October and December 2019. For five sources, we targeted the [C II] emission line, falling in Band 7 at $5 < z < 5.8$. The redshift of two sources ($z \sim 5.9$; J2228+0110 and J2053+0047) places their [C II] line close to the gap between Bands 6 and 7; hence, in these cases, we targeted the CO(6-5) emission line, recovered in Band 3. We chose a compact configuration C(43-2) to avoid flux losses, with 44 antennas used. We centered two spectral windows, slightly overlapping, on the expected observed frequency of the [C II] or CO(6-5) emission line. The remaining two spectral windows were placed to recover the continuum emission at slightly different frequencies. A bandwidth of 1.875 GHz was covered per spectral window. The data were reduced with CASA (McMullin et al. 2007) pipeline for ALMA (version 6.2.1–7), with a standard configuration. The cubes were imaged using the CASA task `tclean` with weighting and robust parameters set to 'briggs' and '2', respectively, to maximize the signal-to-noise ratio (S/N), following similar works from the literature (Decarli et al. 2018). We produce cubes with a spectral resolution width of 30 km s^{-1}. The typical rms noise per 30 km s^{-1} channel is ∼0.50 mJy beam^{-1}, with a typical synthesized beam size of 1.″35 × 1.″10. Below, we report notes on individual objects in the sample and further details on their observations.

2.1. J0131–0321

Yi et al. (2014) discovered this very luminous source ($i = 18.47$) by cross-matching the Sloan Digital Sky Survey (SDSS) Data Release 7 (Schneider et al. 2010) and the Wide-Field Infrared Survey Explorer (WISE; Wright et al. 2010) catalogs, with further confirmation via spectroscopic observations at the Lijiang 2.4 m telescope, and with the Magellan Echellette (MaGE) and the Folded-port InfraRed Echellette (FIRE) Spectrographs at the Magellan telescope. By fitting the Mg II emission line and underlying continuum emission, the authors estimated a redshift of $z = 5.18 \pm 0.02$, a large black hole mass of $2.7 \times 10^9\ M_\odot$, and a bolometric luminosity of $L_{\rm bol} \sim 10^{48}$ erg s^{-1}, with a resulting super-Eddington rate of ∼3.14. Given a radio flux density of 33 mJy at 1.4 GHz, this source presented a high value for the radio loudness parameter of ∼100. Ghisellini et al. (2015) highlighted the potential blazar nature of J0131–0321 with *Swift*-XRT X-ray observations. Fitting its SED with an accretion disk + torus + jet model, these authors estimated a viewing angle of 3–5 deg, and a black hole mass of $\sim 10^{10}\ M_\odot$ (with a factor of ≳2 of systematic uncertainty), allowing for a sub-Eddington accretion rate of ∼0.8. High-resolution Very Long Baseline Interferometer (VLBI) observations with the European VLBI Network (EVN) at 1.7 GHz, obtained by Gabanyi et al. (2015), showed a compact source with high brightness temperature ($T_{\rm B} < 10^{11}$ K) and moderate Doppler boosting factor (≳6). Moreover, they noted a strong radio flux variability with respect to the FIRST survey, supporting the blazar hypothesis. Finally, this source was observed with the uGMRT at 323 MHz, but radio frequency interference contaminated the data, preventing any measurements from being taken (Shao et al. 2020). Nevertheless, using observations at 150 MHz from the TIFR GMRT Sky Survey (TGSS; Intema et al. 2017), the authors were able to estimate a radio power law slope of $\alpha_\nu \sim 0.3$ (with $S_\nu \propto \nu^\alpha$).

J0131–0321 was observed with ALMA on 2019 Nov 28, with a total on-source exposure time of 726 s. The synthesized beam size is 1.″06 × 0.″94, with a position angle (PA) of 82 deg. The rms noise on 30 km s^{-1} channels is 0.49 mJy beam^{-1}.

2.2. PSO055–00

This quasar was selected by mining the Panoramic Survey Telescope and Rapid Response System (Pan-STARRS) and FIRST surveys, and confirmed by spectroscopic follow-up with Palomar/Double Spectrograph (DBSP) and the Very Large Telescope (VLT) FOcal Reducer/low dispersion Spectrograph 2 (FORS2; Bañados et al. 2015b). A reduced χ^2 fit of the observed spectrum to a composite high−z quasar template yielded a redshift of $z = 5.68 \pm 0.05$. PSO055–00 presents a radio flux density at 1.4 GHz of 2.14 ± 0.14 mJy, as obtained from the FIRST Survey, and a radio loudness parameter of $R_{2500} = 83 \pm 9$ (Bañados et al. 2021).

Our ALMA observations of this quasar were obtained on 2019 Dec 17 with a total on-source exposure time of 816 s. The measured rms noise is 0.54 mJy beam^{-1} on 30 km s^{-1} channels, while the beam size is 1.″39 × 1.″05, with PA = 81 deg.

2.3. PSO135+16

PSO135+16 was selected as a high−z quasar candidate in a similar fashion as PSO055–00. It was then confirmed spectroscopically with the Large Binocular Telescope (LBT) Multi-Object Double Spectrograph (MODS) and VLT/FORS2 (Bañados et al. 2015b). It is located at $z = 5.68 \pm 0.05$, as measured by fitting its spectrum to a reference template. Its radio loudness parameter is $R_{2500} = 177 \pm 18$, with a radio flux density of $f_{1.4\,\mathrm{GHz}} = 3.04 \pm 0.15$ mJy, as obtained from the FIRST survey.

ALMA observed PSO135+16 on 2019 Dec 02 with exposure time of 1058 s. The beam size is of $1\farcs39 \times 1\farcs21$, PA = −30 deg, and the rms noise is of 0.50 mJy beam^{-1} on 30 km s^{-1} channels.

2.4. J1034+2033

This bright ($z = 19.79$) source was firstly presented as part of the SDSS-DR7 quasar catalog (Schneider et al. 2010). It is located at a redshift of $z = 5.01$[2] (Pâris et al. 2018). J1034+2033 has a radio flux density $f_{1.4\,\mathrm{GHz}} = 3.96 \pm 0.15$ mJy, from the FIRST survey, and a radio loudness parameter of $R_{2500} = 47 \pm 4$. Shao et al. (2020) observed J1034+2033 with the uGMRT, measuring a flux density of 2.97 ± 0.19 mJy at 323 MHz, and fitting a radio spectral slope of $\alpha_\nu \sim 0.18$.

Our ALMA data for this quasar were obtained on 2019 Dec 04, with a rms noise of 0.78 mJy beam^{-1} on 30 km s^{-1} channels, and a beam size of $1\farcs36 \times 1\farcs04$, PA = −33 deg. The total exposure time was 1058 s.

2.5. J2228+0110

Zeimann et al. (2011) selected J2228+0110 as a quasar candidate by cross-matching the Stripe82 SDSS and Stripe 82 VLA surveys. Its high−z quasar nature was confirmed by observations with the Keck/LRIS spectrograph. J2228+0110 is optically faint (with an observed magnitude $z = 22.3$), with a radio flux density of $f_{1.4\,\mathrm{GHz}} = 0.31 \pm 0.06$ mJy and a radio loudness parameter of $R_{2500} \sim 70$. A tentative detection of a Lyman Alpha Halo (LAH) around this quasar was firstly presented by Roche et al. (2014), using the Gran Telescopio Canarias (GTC)-Optical System for Imaging and low-Intermediate-Resolution Integrated Spectroscopy (OSIRIS) long-slit spectroscopy. Deep (11 h) MUSE observations confirmed the presence of an extended (∼6″.0, i.e., ∼30 pkpc at $z \sim 6$) and bright ($\sim 2 \times 10^{-16}$ erg s^{-1} cm^{-2}) LAH towards the south-east direction (Drake et al. 2019, Farina et al. 2019). ALMA targeted J2228+0110 on 2019 Oct 12, with an exposure time of 3810 s. The measured rms noise is 0.32 mJy beam^{-1} on 30 km s^{-1} channels, and the beam size is $1\farcs44 \times 1\farcs28$, PA = −78 deg.

2.6. PSO352–15

Bañados et al. (2018b) selected PSO352–15 as a quasar candidate from the Pan-STARRS survey, confirming it with spectroscopic observations using Magellan/Low Dispersion Survey Spectrograph (LDSS3). This quasar was initially located at $z = 5.84$, via a template fit, and is optically faint ($z = 21.22$). With very bright radio flux density measurements from available radio surveys and dedicated VLA follow-ups, it is one of the most radio-loud sources at $z > 5$. Further high-resolution radio observations with the Very Long Baseline Array (VLBA) resolved the source into different components with a spatial extension of ∼1.3 kpc and a morphology consistent with a one-sided jet or a compact symmetric object (Momjian et al. 2018). Rojas-Ruiz et al. (2021) presented a collection of multi-wavelength observations for this source, included ALMA data collected as part of this program. They re-calculated the radio loudness parameter as $R_{2500} \sim 1350$ and showed evidence for a break in the radio spectral distribution. Intriguingly, they found signs for synchrotron emission contribution down to the rest-frame infrared (IR) regime (see also Sect. 4.3 below). We still report PSO352-15 here as part of the RL sample, although we re-calculated its properties for consistency (see Sect. 3). This object was observed on 2019 Nov 28, with an exposure time of 756 s. We measured a rms noise of 0.58 mJy beam^{-1}, and a beam size of $1\farcs27 \times 1\farcs00$, PA = 86 deg.

2.7. J2053+0047

This faint ($z = 21.41$) quasar at redshift $z = 5.92$ was selected by Jiang et al. (2009) using SDSS survey data. Bañados et al. (2015b) identified a 3σ detection in the FIRST survey data, with a radio flux density of $f_{1.4\,\mathrm{GHz}} = 434 \pm 143\,\mu$Jy, obtaining a radio loudness parameter of ∼44, signaling this as a RL quasar. Deeper observations with the VLA provided new flux density limits of $f_{1.4\,\mathrm{GHz}} \sim 13\,\mu$Jy, yielding an upper limit on the radio loudness parameter as low as <9.7 (Liu et al. 2021). Hence, J2053+0047 has been currently reclassified as a RQ source. We still report the data collected for this source here for completeness. Our ALMA observations of this source were obtained on 2019 Oct 13. The total exposure time was 2570 s, and we measure a beam size of $1\farcs56 \times 1\farcs20$, PA = 65 deg, and rms noise of 0.23 mJy beam^{-1}.

3. Results

Here, we describe our steps to recover the properties of the [C II], CO(6-5) emission lines and the underlying dust continuum.

3.1. [CII] line measurements

We targeted the [C II] emission line in five quasars: J0131-0321, PSO055-00, PSO135+16, J1034+2033, and PSO352-15. To properly account for potentially extended sources, we extracted our one dimensional (1D) spectrum for each source in an aperture centered on the quasar position (e.g., Novak et al. 2019, Rojas-Ruiz et al. 2021). We determined the best aperture by extracting the flux of the quasars in concentric apertures from 0″.1 up to 3″.0 and choosing the radius at which the flux encounters a plateau. Once the best aperture is found, we extracted the one dimensional spectra and fit them with a flat continuum and a Gaussian line. We detected the [C II] emission line in all sources. The emission line for the quasar PSO055-00 was found at the edge of the bandwidth: this is due to the large uncertainty of the literature redshift derived from template fit of the rest-frame UV spectrum. Therefore, caution should be taken when considering its [C II] emission line value and the derived quantities. We report the 1D spectra in Fig. 1 and the values of the fit and apertures radii in Table 2.

We created continuum-subtracted [C II] emission line cubes in the following way. We chose the line spectral windows centered on the frequency peak of the Gaussian fit and width corresponding to $\pm 1.4\sigma$; this recovers ∼83% of the total line flux

[2] We considered here the redshift from visual inspection and as uncertainty the corresponding dispersion of Z_VI–Z_MGII. All the other redshift measurements in this case are consistent with the reported value within the uncertainty.

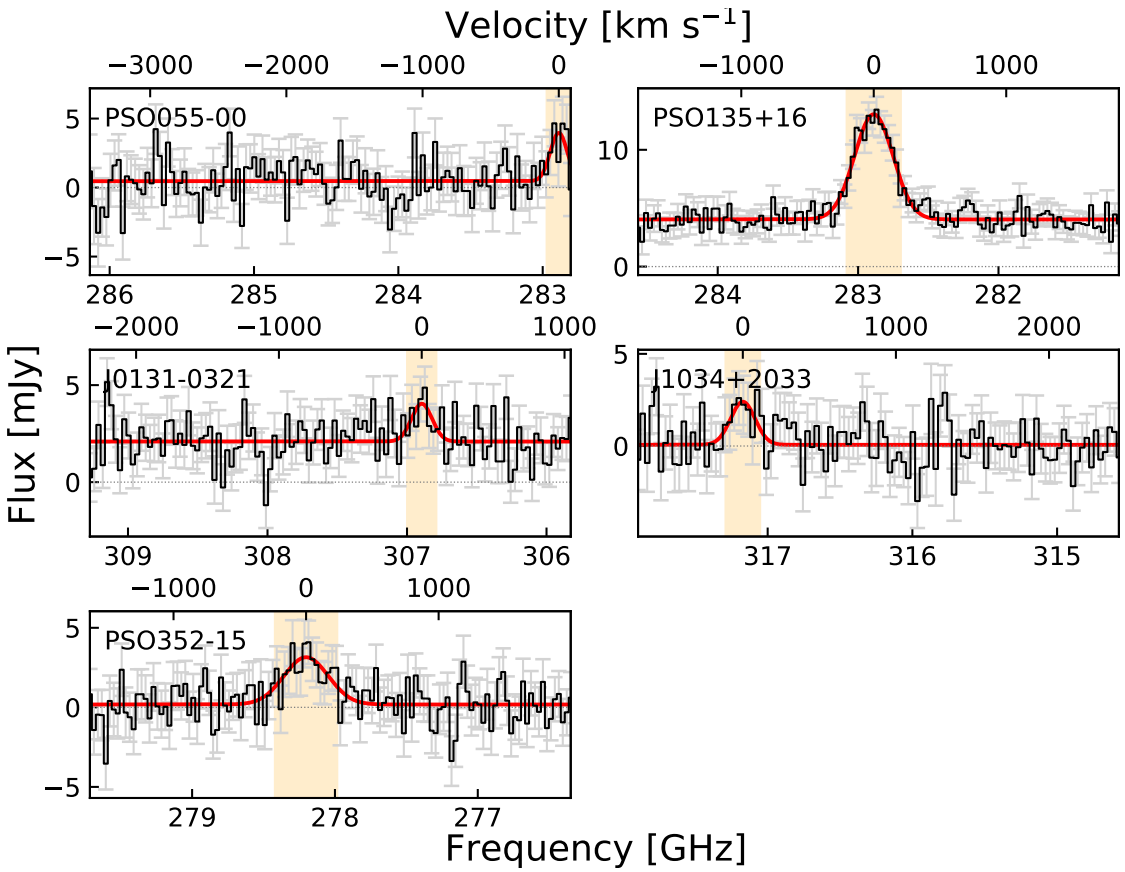

Fig. 1. ALMA [C II] emission line and underlying continuum of the quasars in our sample, re-sampled to 30 km s^{-1} velocity bin, considering extraction apertures of different radii (see Sect. 3.1 and Table 2). The error (light grey) is obtained by taking the pixels rms and re-scaling the values considering the number of pixels in the aperture and the beam size. The continuum + Gaussian fit is plotted with a red solid line. We show the channels used to extract the continuum-subtracted [C II] maps ($\pm 1.4\sigma$) with yellow shading (see Sect. 3.1).

Table 2. Results from spectral fit of the sources observed in Band 7.

Name	$\nu_{\rm obs}$ ([C II]) [GHz]	z ([C II])	FWHM ([C II]) [km s^{-1}]	$F_{\rm line}$ ([C II]) [Jy km s^{-1}]	$F_{\rm cont}$ [mJy]	$r_{\rm aper}$ [″]
J0131-0321	306.895 ± 0.03	5.1928 ± 0.0006	170 ± 70	0.35 ± 0.20	2.10 ± 0.10	1.4
PSO055-00 $^{(\star)}$	283.889 ± 0.02	5.7183 ± 0.0005	150 ± 60	0.55 ± 0.30	0.46 ± 0.20	2.3
PSO135+16	282.889 ± 0.008	5.7183 ± 0.002	340 ± 29	3.30 ± 0.30	4.00 ± 0.10	1.6
J1034+2033	317.172 ± 0.03	4.9921 ± 0.0005	190 ± 80	0.47 ± 0.30	0.064 ± 0.10	1.3
PSO352–15	278.202 ± 0.03	5.8315 ± 0.0007	390 ± 90	1.20 ± 0.040	0.18 ± 0.20	1.7

Notes. The spectra were extracted from different apertures ($r_{\rm aper}$; see Sect. 3.1). $^{(\star)}$We note that PSO055-00's line emission is recovered at the edge of the bandwith. Therefore, caution should be taken when considering its [C II] emission line value and all derived quantities.

and maximizes the S/N, in case of a perfectly Gaussian line profile (e.g., Decarli et al. 2018, Novak et al. 2020, Appendix A). The continuum subtraction is done in the *uv* space using the CASA task *uvcontsub*. We then re-imaged the continuum subtracted cubes with `tclean`, with robust = 2. We reported the [C II] continuum-subtracted moment-0 maps in Fig. 2. We fit the continuum-subtracted [C II] map with a 2D Gaussian function within CASA, selecting a small rectangular region around the source. We reported the flux values and sizes of the sources in our sample in Table 4. We note that the maps are built considering only 83% of the total line flux; therefore, the 2D flux need to be corrected by a factor of ∼1.20 (e.g., Decarli et al. 2018). We made a first order assessment of the kinematics of these sources (see Appendix A). However, due to the low S/N and limited spatial resolution of the maps, we were not able to draw stronger conclusions on their kinematics. Thus, additional deeper and higher resolution observations are needed. It is worth noting that our results for the quasar PSO352-15 are consistent with those presented in Rojas-Ruiz et al. (2021). We refer to this work for further insights in the morphological study of this source. In the remainder of the paper, we use the [C II] emission line flux obtained by the 2D Gaussian fit, corrected by a factor of 1.20.

3.2. CO(6-5) line measurements

Observations in Band 3, targeting the CO(6-5) emission lines, were obtained for two quasars: J2228+0110 and J2053+0047.

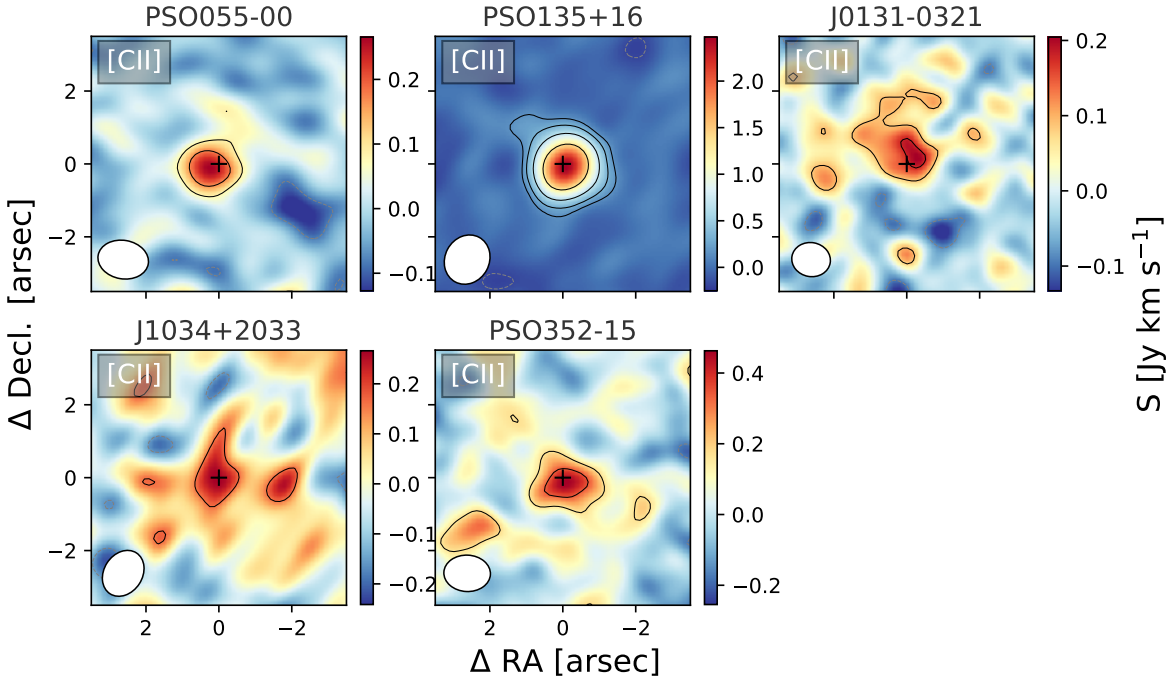

Fig. 2. ALMA continuum-subtracted [C II] maps. The continuum black/dashed grey contours highlights the $\pm 2\sigma$, 4σ, 8σ.. levels. The beam size is shown with a white ellipse, while the rest-frame UV/optical position of the quasar is reported with a black cross. The morphology of all the sources is broadly consistent with the beam size; hence, we consider them to be unresolved at the spatial resolution and S/N of this dataset.

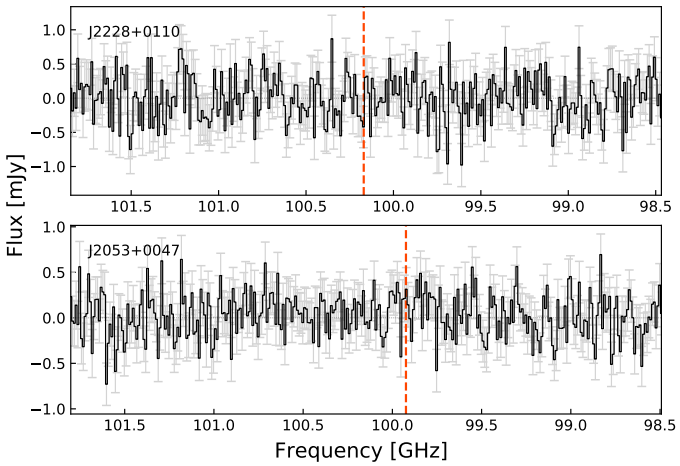

Fig. 3. ALMA spectra of J2228+0110 and J2052+0047 observed in Band 3. No continuum nor CO(6-5) emission lines were detected. The expected locations of the CO(6-5) line at the redshifts of the quasars are shown with orange dashed lines.

No clear emission was seen in the reduced cubes. We extracted the 1D spectrum from the central pixel, namely, at the nominal position of the quasar. No line nor continuum emission were detected.

We can place upper limits to the continuum emission at 2σ by considering the mean rms noise on the extracted 1D spectrum. We also estimated upper limits on the emission line flux at 3σ, considering a typical line width of 300 km s^{-1} (e.g., Decarli et al. 2022). We show in Fig. 3 the extracted 1D spectra. In Table 3, we give the continuum and CO(6-5) emission line flux limits.

Table 3. Limits on the continuum and CO(6-5) emission line fluxes (see Sect. 3.2) and derived limits on the line and IR luminosities (see Sect. 4.5).

Name	J2228+0110	J2053+0047
$F_{\rm CO(6-5)}$ [Jy km s^{-1}]	<0.68	<0.53
$F_{\rm cont,690\,GHz}$ [mJy]	<0.64	<0.47
$L_{\rm CO(6-5)}$ [$10^8\,L_\odot$]	<2.4	<1.9
$L'_{\rm CO(6-5)}$ [$10^{10}\,L_\odot$]	<2.2	<1.8
$L_{\rm FIR}$ [$10^{12}\,L_\odot$]	<46	<34
$L_{\rm TIR}$ [$10^{12}\,L_\odot$]	<67	<50

3.3. Continuum measurements

We recovered the continuum emission at $\nu_{\rm rf} \sim 1900$ GHz and $\nu_{\rm rf} \sim 1970$ GHz in Band 7 in the lower and upper side bands, respectively. In the case of Band 3, we targeted the continuum at $\nu_{\rm rf} \sim 690$ GHz (lower) and $\nu_{\rm rf} \sim 620$ GHz (upper side band).

We estimated the continuum properties for the sources observed in Band 7 as follows. We created pure continuum maps for the lower and upper side bands by collapsing the frequency channels not incorporating the [C II] emission line (see Sect. 3.1). In both cases, the continuum emission was recovered in all the sources. We modeled each continuum emission from the maps with a 2D Gaussian function, using CASA. The measured sizes are consistent with the beam size. We produced similar continuum maps for the two sources observed in Band 3, but no emission was recovered in either case.

We report the continuum flux density and size values for observed Band 7 emission in Table 4 and give limits on non-detections in Band 3 in Table 3. The continuum maps are shown in Figs. 4 and 5. For the remainder of the paper, to calculate the

Table 4. Results of the 2D Gaussian fit of the continuum maps and the [C II] continuum-subtracted emission line maps for the sources observed in Band 7.

Name	Size$_{[C\,II]}$ [″]	Size$_{1900\,GHz}$ [″]	Size$_{1970\,GHz}$ [″]	$F_{[C\,II]}$ [Jy km s^{-1}]	$F_{[C\,II],corr}$ [Jy km s^{-1}]	$F_{cont,1900\,GHz}$ [mJy]	$F_{cont,1970\,GHz}$ [mJy]
J0131−0321	1.660 × 1.140	1.120 × 0.982	1.205 × 1.035	0.398 ± 0.079	0.480 ± 0.095	2.130 ± 0.056	2.176 ± 0.090
PSO055−00 (⋆)	1.314 × 1.148	1.713 × 1.300	1.566 × 0.908	0.281 ± 0.023	0.339 ± 0.028	0.586 ± 0.027	0.386 ± 0.043
PSO135+16	1.352 × 1.261	1.352 × 1.245	1.295 × 1.179	2.504 ± 0.092	3.017 ± 0.111	4.42 ± 0.16	4.510 ± 0.15
J1034+2033	1.560 × 1.120	1.044 × 0.867	1.52 × 1.12	0.345 ± 0.034	0.416 ± 0.041	0.168 ± 0.030	0.231 ± 0.045
PSO352−15	1.614 × 1.184	1.280 × 0.897	1.91 × 1.30	0.695 ± 0.093	0.837 ± 0.112	0.300 ± 0.031	0.581 ± 0.098

Notes. The corrected flux is obtained by considering a 1.20 factor (see Sect. 3.1). The (not deconvolved) size measurements provided here are consistent with the beam sizes. (⋆)We note that PSO055-00's line emission is recovered at the edge of the bandwith. Therefore, caution should be taken when considering its [C II] emission line value and all derived quantities.

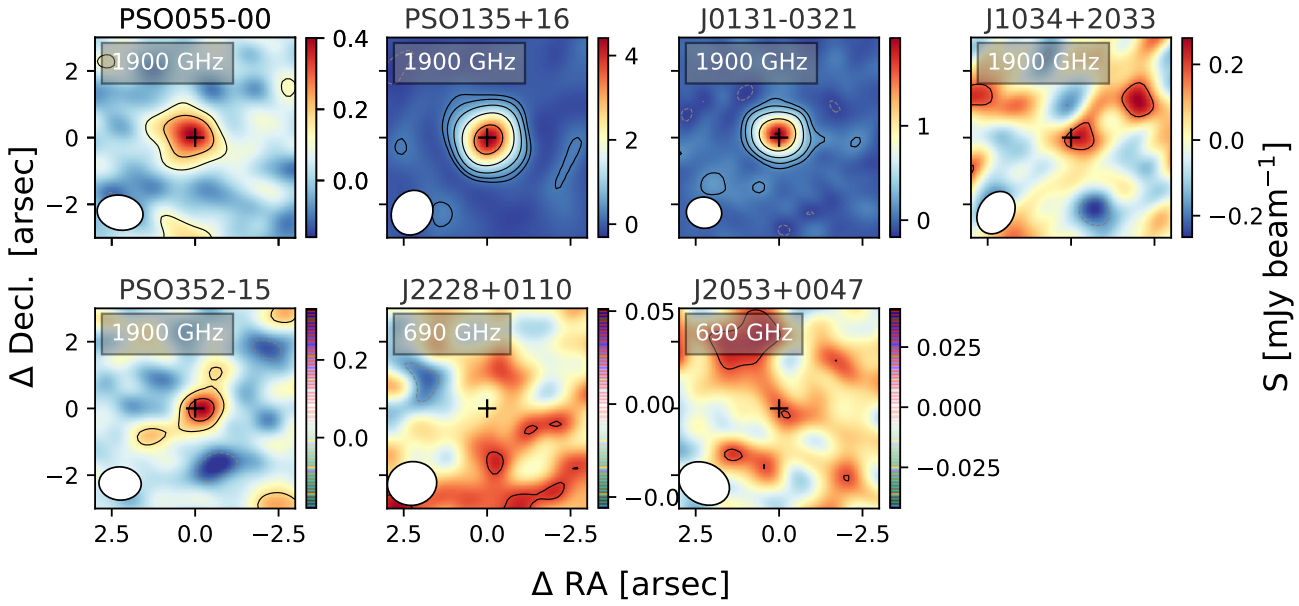

Fig. 4. ALMA continuum emission maps at rest-frame 1900 GHz (Band 7) and 690 GHz (Band 3). The black solid and dashed grey contours indicate the ±2, 4, 8..σ levels. We show the synthesized beam in white in the left bottom of each panel. The rest-frame UV/optical position of the quasar is reported with a black cross. The continuum emission is not detected in J2228+0110 nor in J2053+0047.

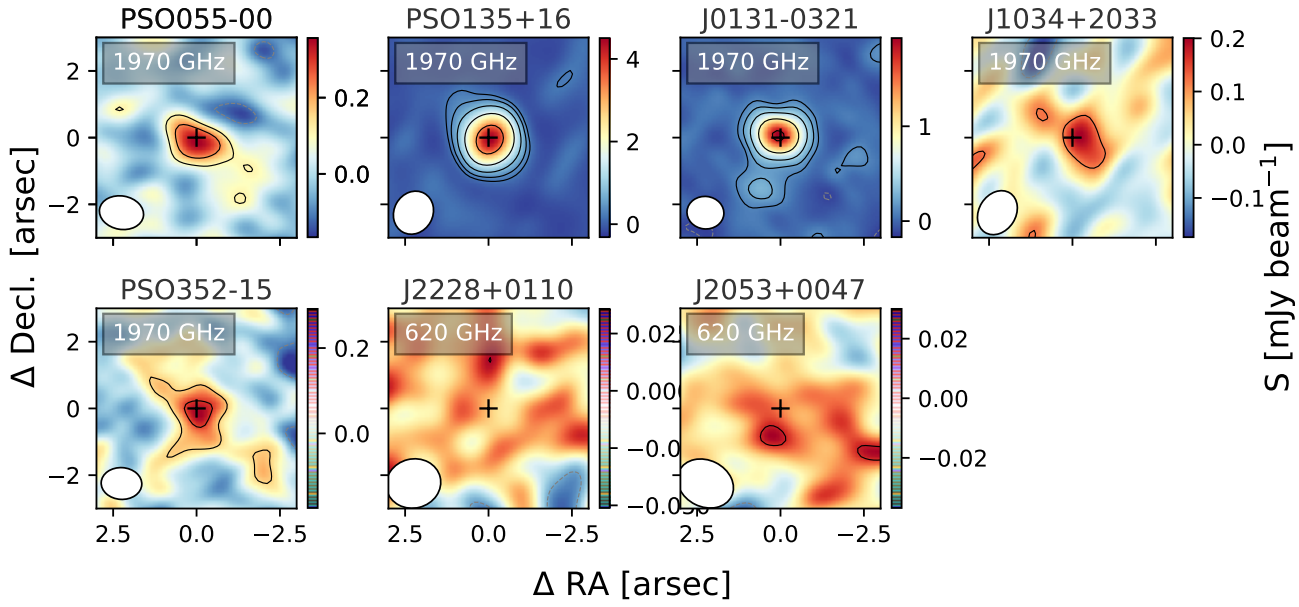

Fig. 5. ALMA continuum emission maps at rest-frame 1970 GHz (Band 7) and 620 GHz (Band 3). Symbols as in Fig. 4.

corresponding IR quantities (see Sect. 4), we use the continuum emission flux obtained at 1900 GHz from the 2D Gaussian fit ($F_{\rm cont,1900\,GHz}$), reported in Table 4.

4. Analysis

Here, we report gas and dust properties derived from the measurements of our RL quasar sample. We also compare them with those of RQ quasar hosts at similar redshift taken from the literature.

4.1. Literature sample

In this work we compare the properties of RL quasars host galaxies with those derived from the literature. For the RQ sample, we considered sources from the following studies, which targeted their dust continuum and [C II] emission line: Walter et al. (2009), Wang et al. (2013, 2016), Willott et al. (2013, 2015, 2017), Mazzucchelli et al. (2017), Trakhtenbrot et al. (2017), Decarli et al. (2018), Izumi et al. (2018, 2019, 2021), Venemans et al. (2020), Nguyen et al. (2020), Yang et al. (2020), and Eilers et al. (2020, 2021). The total number of RQ sources is 76.

We also consider six additional RL quasar host galaxies' properties from the literature. Four of these come from Khusanova et al. (2022): J0309+2717 (z = 6.115), J1427+3312 (z = 6.115), J1429+5447 (z = 6.1845), and PSO172+18; the latter is a potentially very young radio source at z = 6.823, Momjian et al. (2021), for which only upper limits in both continuum and [C II] emission lines have been obtained. The fifth source is J2318-3113 (z = 6.44), which was re-classified as a RL quasar by Ighina et al. (2021). Using new 888 MHz radio observations acquired with the Rapid ASKAP Continuum Survey (RACS; McConnell et al. 2020, Hale et al. 2021) they obtained a new radio loudness parameter of $R_{4400} \sim 70$ and observed a potential flux density variability of a factor of ∼2 in one year. In a recent study, Ighina et al. (2024) presented new, multi-wavelength (radio, optical/NIR, X-ray) data, which reinforced the scenario of a young radio source with a black hole mass of $\sim 8 \times 10^8\,M_\odot$. Here, we adopt $R_{2500} = 152$ and a spectral index of $\alpha = 0.54$ reported by Ighina et al. (2021). J2318-3113 had been previously observed with ALMA by Decarli et al. (2018) and Venemans et al. (2020). We include J2318-3113 in our RL quasar sample, utilizing the measurements provided by Venemans et al. (2020). Finally, we included a very recently discovered blazar at z = 6.9964, namely, J0410-0139 (Banados et al. 2024a). Here, we consider the continuum and [C II] emission line fluxes from ALMA Band 6 observations obtained in August 2022 (Banados et al. 2024b). For all the sources from the literature, we re-derived the IR and [C II] luminosities, SFRs, and dust masses consistently with the objects presented in this work, as outlined in Sect. 4.4.

4.2. Redshift estimations

We estimate the redshifts of the quasars in our sample from the peak of the [C II] emission line and we report these values in Table 2. Several studies (e.g., Venemans et al. 2017a, Decarli et al. 2018, Meyer et al. 2019, Schindler et al. 2020) have highlighted a systematic, high blueshift of the rest-frame UV emission lines (e.g., C IV, Mg II), with respect to lines arising from the ISM in the host galaxy, considered the rest-frame of the system. Moreover the Lyα emission line at high-redshift is known to provide a poor estimation of the quasar redshift, due to effects introduced by the absorption of the intergalactic medium (IGM; e.g., Bañados et al. 2016). Here, we find that the blueshift for J0131-0321, the only quasar whose redshift was known from the Mg II emission line, is very small (i.e., $\Delta v_{\rm Mg\,II-[C\,II]} = -127\,{\rm km\,s^{-1}}$). This is consistent with the median difference of $\Delta v_{\rm Mg\,II-[C\,II]}$ observed in the literature for RQ quasars ($\sim -367/-390\,{\rm km\,s^{-1}}$ at $z \sim 5/6$, Nguyen et al. 2020 and Schindler et al. 2020). However, the blueshift relative to our [C II] redshifts for the cases of literature redshifts based on observations of the Lyα emission line or from template fitting are much larger, with a maximum value of $-2060\,{\rm km\,s^{-1}}$ (for PSO055-00, which is indeed recovered at the edge of the bandwidth). We measured a mean, median, and standard deviation for $\Delta v_{\rm Ly\alpha/temp-[C\,II]}$ of −1269, −770, and 2271 ${\rm km\,s^{-1}}$, respectively.

4.3. Radio and (sub)mm spectral energy distribution

We set our ALMA measurements of the continuum emission in the context of the spectral energy distribution (SED) of the RL quasars studied here. We utilized radio measurements from the literature (Zeimann et al. 2011, Bañados et al. 2018b, Shao et al. 2020, 2022, Rojas-Ruiz et al. 2021, Krezinger et al. 2024) that had been obtained either via dedicated follow-up with VLA, VLBI, uGMRT, and/or NOEMA, or drawn from the FIRST and TGSS surveys. In addition, we obtained new measurements from RACS and the ASKAP First Large Absorption Survey in HI (ASKAP-FLASH; Allison et al. 2022). In practice, we downloaded from CASDA[3] the available images of the quasars PSO055-00, PSO135+16, and J1034+2033. We fit a Gaussian profile within CASA to obtain the integrated fluxes at observed frequencies 0.89 GHz and 1.37 GHz (RACS) and at 0.86 GHz (FLASH). We note that the various reported observations were obtained in different times, within days to several years from each other; hence, the radio-intrinsic SED shape might be altered by variability effects. The resulting SEDs are shown in Fig. 6.

In general, quasar SEDs at radio frequencies are dominated by synchrotron emission, which can be modeled with a power law ($S_\nu \propto \nu^\alpha$). In the case of PSO352-15, a broken power-law with $\alpha_3^{0.215} = -0.88 \pm 0.08$ (measured between observed frequencies 0.215 and 3 GHz) and $\alpha_{100}^{3} = -1.26 \pm 0.03$ (measured between observed frequencies 3 and 100 GHz) is better at reproducing the data; for a detailed discussion on this source, we direct the reader to Rojas-Ruiz et al. (2021). We highlight that by extrapolating the sole synchrotron emission, we would obtain at the observed ALMA frequency a flux of ∼0.027 mJy (see Fig. 6). Consequently, the estimated synchrotron contribution for this source is of ∼9%, as discussed in Rojas-Ruiz et al. (2021).

J0131-0321 and J1034+2033 were extensively observed with the VLA and uGMRT by Shao et al. (2020) and (2022). A turn-over of the radio spectra was recovered, around an observed (rest-frame) frequency of ∼2 (∼10) GHz in J0131-0321, and of ∼4 (∼20) GHz in J1034+2033. Such radio spectral shapes are typically observed in GHz-peaked sources (GPS) or high-frequency peakers (HFP). Shao et al. (2022) shows that a model of free-free absorption by an external, in-homogeneous medium can best reproduce both cases. We report in Fig. 6 the corresponding, approximate power-law emission at frequencies higher than the turn-over, with the slopes indicated by Shao et al. (2022), which we can extrapolate to the frequencies of our dust emission model. We note that in the case of J0131-0321, virtually most of the emission we recover from

[3] https://data.csiro.au/domain/casda

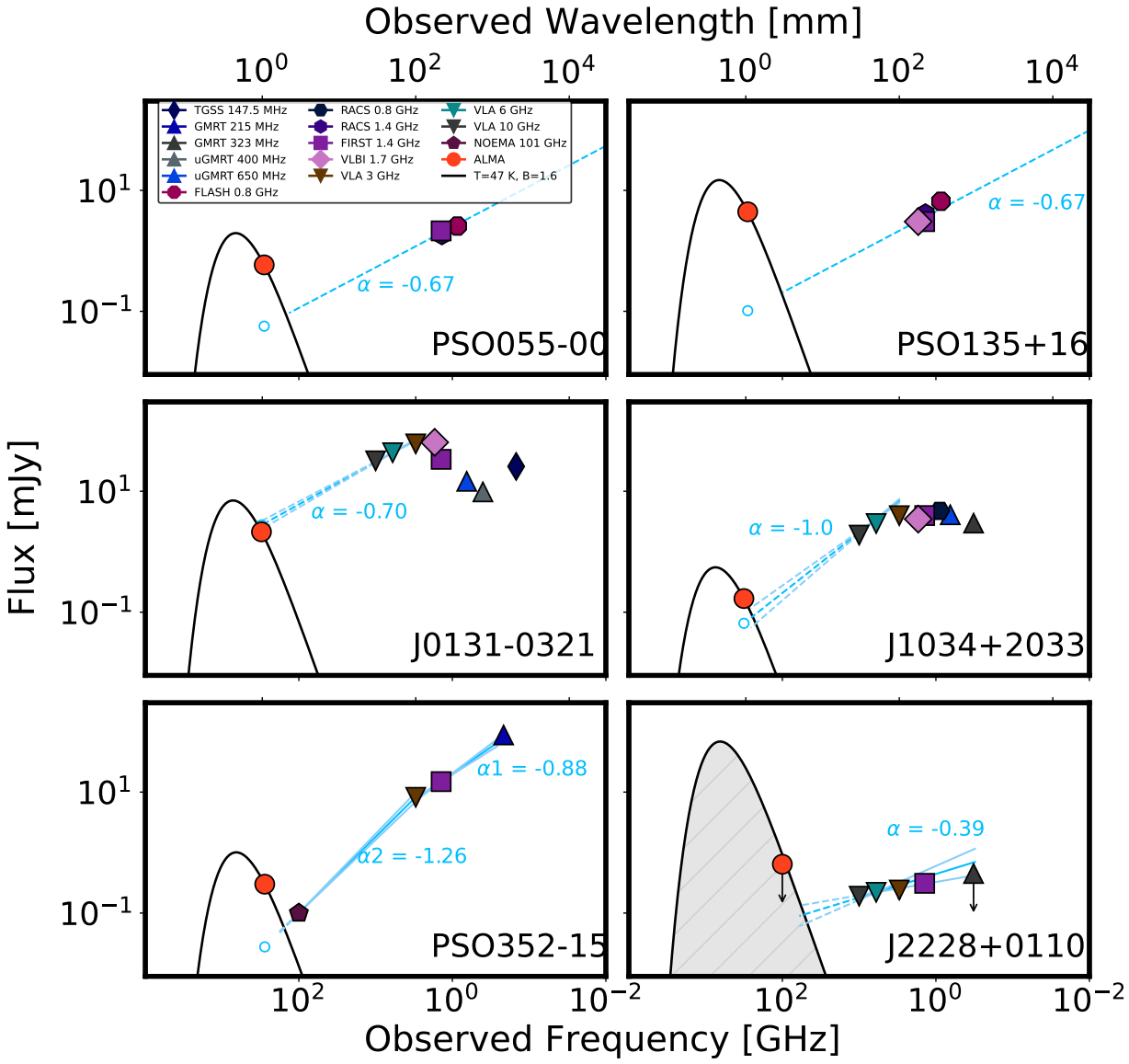

Fig. 6. Radio and (sub)mm spectral energy distributions (SED) of RL quasars reported in this work. We show the continuum emission at 1 mm from our ALMA Band 7 observations (orange circles) and the relative best fit of the modified black body dust emission (black line). In the case of J2228+0110, we could retrieve only upper-limits from our ALMA Band 3 data and we show the corresponding limits on its dust emission with a shaded grey area. All modified black-body are calculated with T = 47 K and $\beta = 1.6$ (see Sect. 4.4). For each quasar, we report the radio observations obtained from a collection of literature data (see Sect. 4.3 for references). For J0131-0321, J1034+2033, PSO352-15, J2228+0110 we show (broken) power-law radio emissions, with slopes (α) derived from fits in the literature. For PSO055-00, PSO135+16, we assume a median high−z slope value (see Sect. 4.3). The solid light blue lines are the measured power-law functions, while we report with dashed lines the extrapolation to lower and higher frequencies. The light cyan lines highlight the regions encompassed by the 1σ uncertainties on the power-law slopes. We show with light blue empty circles the flux extrapolated from the synchtrotron power-law functions at the ALMA frequency targeted in this work.

our ALMA continuum observations at observed 300 GHz could be due to synchrotron emission. For J1034+2033, the recovered intensity measured with ALMA (0.168 mJy; see Table 4) is higher than what is expected by the sole synchrotron emission extrapolation (~0.065 mJy; see Fig. 6). In both cases, a mix of dust + synchrotron radiation could be responsible for the continuum emission observed with ALMA. In particular, extrapolating the radio power-law, we can obtain a first order estimate of synchrotron contribution at ~300 GHz of ~40% and ~100% for J1034+2033 and J0131-0321, respectively.

J2228+0110 is the weakest radio emitter in this sample. It was observed with VLA and uGMRT by Shao et al. (2020), and (2022); in contrast to J0131-0321 and J1034+2033, no clear radio turn-over was observed, although the upper limits recovered with the uGMRT could provide a hint of a change in the spectrum. If we do not consider this upper limit, the radio emission could be modeled, between the observed frequencies of 323 MHz and 1 GHz, with a relatively flat power law and $\alpha = -0.39 \pm 0.17$. This object was also not detected in our ALMA Band 3 observations; hence, we only have upper limits for its continuum emission, shown in gray shading in Fig. 6.

PSO055-00 and PSO135+16 were observed only within 0.8–1.7 GHz; hence, a model of their radio emission cannot be meaningfully fitted; we show in Fig. 6 an indicative power law

emission with a slope of $\alpha = -0.67$, used in Bañados et al. (2021) to derive their radio-loudnesss parameters; it is calculated as the median slope of the radio emission in $z > 5$ quasars. In both cases, this slope is broadly consistent with the radio measurements and we do not observe strong variability. Our ALMA measurements (0.586 mJy and 4.42 mJy for PSO055-00 and PSO135+16, respectively; see Table 4) are approximately one order of magnitude higher than the flux density obtained when extrapolating the synchrotron emission (~0.057 mJy and ~0.102 mJy for PSO055-00 and PSO135+16, respectively; see Fig. 6). In this case, the estimated synchrotron contribution at ~300 GHz are ~9% and ~2% for PSO055-00 and PSO135+16, respectively.

All these lines of evidence show the variety of the SEDs of high−z RL quasars and highlights how observations at rest frame of ~1 mm, in the case of RL quasars, could be the result of thermal and non-thermal emission. Therefore, extreme caution should be used when deriving SFR, dust and gas masses, from continuum measurements at these wavelengths. To continue to provide valuable estimates, discussions, and comparisons with the literature, while considering the above described limitations with the currently available datasets, we derived such quantities in two ways. We first consider the total ALMA recovered continuum data as purely produced by dust, which will provide upper limits to IR luminosities, SFR, and dust/gas masses. Secondly, we derived these measurements by subtracting the synchrotron values as extrapolated at ~1 mm from the radio power-law functions (as described above) to the total observed ALMA continuum flux. Considering that the radio power-law functions are expected to bend downward towards higher frequencies due to the interaction between high-energy particles in the jets and the surrounding medium (e.g., Jaffe & Perola 1973), decreasing the synchrotron contribution, the IR-related quantities derived in this way can be considered as the lower limits. The intrinsic SFR, IR luminosities and gas/dust masses should then be found within the two reported values. Given that virtually ~100% of the ~300 GHz flux density of J0131-0321 could be due to synchrotron, we did not derive a second measure for this source; instead, we considered the initially derived IR values as the pure upper limits. Also, we did not derive a second set of values for J2228+110, as we recovered only the upper limits from our ALMA data. Further observations at intermediate frequencies are needed to properly model these RL quasars SED, as well as to more accurately and quantitatively retrieve all their components.

4.4. IR and [C II] luminosities, star formation rates and dust masses

We can estimate the [C II] line luminosity from the measured velocity-integrated line flux, following Carilli & Walter (2013):

$$\frac{L_{[\rm CII]}}{L_\odot} = 1.04\times10^{-3}\frac{F_{[\rm CII]}}{\rm Jy\,km\,s^{-1}}\frac{\nu_{\rm obs}}{\rm GHz}\left(\frac{D_{\rm L}}{\rm Mpc}\right)^2, \quad (1)$$

with $F_{[\rm CII]}$ flux of the [C II] emission line, $\nu_{\rm obs}$ the observed frequency of the line, and $D_{\rm L}$ the luminosity distance.

Meanwhile, the IR emission of high−z quasars can be modeled with a modified black body (e.g., Decarli et al. 2018, Venemans et al. 2018). Hence, in the optically thin scenario, the observed continuum flux density can be derived as follows (e.g., Novak et al. 2019):

$$F_{\rm obs} = \frac{f_{\rm CMB}[1+z]}{D_{\rm L}^2}\kappa_{\nu,\rm rest}(\beta)M_{\rm dust}B_{\nu,\rm rest}(T_{\rm dust},z), \quad (2)$$

where $M_{\rm dust}$ is the dust mass, $T_{\rm dust}$ is the dust temperature and $B_{\nu,\rm rest}(T_{\rm dust},z)$ is the Planck function:

$$B_{\nu,\rm rest}(T_{\rm dust},z) = \frac{2h}{c^2}\nu_{\rm rest}\left[\exp\left(\frac{h_\nu}{kT_{\rm dust}}\right)-1\right]. \quad (3)$$

The factor $\kappa_{\nu,\rm rest}(\beta)$ is the dust mass opacity coefficient (e.g. Dunne et al. 2000), expressed here as

$$\kappa_{\nu,\rm rest}(\beta) = 0.077\left(\frac{\nu_{\rm rest}}{352\,\rm GHz}\right)^\beta \rm m^2\,kg^{-1}, \quad (4)$$

with β as the dust emissivity power law spectral index. At high redshift ($z \gtrsim 5$), the cosmic microwave background (CMB) contrast starts to become significant. We can take into account this correction via the factor $f_{\rm CMB}$ (e.g., da Cunha et al. 2013):

$$f_{\rm CMB} = 1 - \frac{B_{\nu,\rm rest}(T_{\rm CMB,z})}{B_{\nu,\rm rest}(T_{\rm dust,z})}. \quad (5)$$

Here, we consider values for dust temperature and β typically used in the literature, i.e., $T_{\rm dust} = 47$ K and $\beta = 1.6$ (e.g., Beelen et al. 2006, Decarli et al. 2018, Rojas-Ruiz et al. 2021). We scale the above function to the observed continuum flux densities at $\nu_{\rm rest} = 1900$ GHz of our sources (as derived from the 2D Gaussian fit), as well as considering the synchrotron-corrected ones (see Sect. 4.3). Hence, we derive dust masses for our quasar hosts of $<3\times10^8\,M_\odot$.

We calculated the far-infrared (FIR) luminosity ($L_{\rm FIR}$) by integrating the modified black body between rest-frame wavelength 42.5 and 122.5 µm (e.g., Helou et al. 1988). We also estimated the total IR luminosity ($L_{\rm TIR}$) by integrating the SED between 8 and 1000 µm (e.g., Kennicutt & Evans 2012), which is equivalent to $L_{\rm FIR} = 0.75\,L_{\rm TIR}$ for the model considered here.

We also estimate the equivalent width of the [C II] emission line ($\rm EW_{[CII]}$):

$$\frac{\rm EW_{[CII]}}{\rm km\,s^{-1}} = 1000\times\frac{F_{[\rm CII]}\,[\rm Jy\,km\,s^{-1}]}{F_{\rm cont}\,[\rm mJy]}. \quad (6)$$

We can compute the star formation rates in the quasar host galaxies by relying both on the [C II] emission line ($\rm SFR_{[CII]}$) and the IR luminosities ($\rm SFR_{IR}$). Several studies establish a relation between $L_{\rm [C\,II]}$ and star formation rates, for instance, De Looze et al. (2011), Sargsyan et al. (2012), and Herrera-Camus et al. (2015). Here, we can obtain [C II]-derived SFR using

$$\rm SFR_{[CII]} = 3\times10^{-9}\left(\frac{L_{[\rm CII]}}{L_\odot}\right)^{1.18} \quad (7)$$

from De Looze et al. (2014), whose relation was calibrated on $z > 0.5$ galaxies with a scatter of ~0.4 dex. For the dust-based star formation rates we use the equation from Kennicutt & Evans (2012):

$$\frac{\rm SFR_{IR}}{M_\odot\,\rm yr^{-1}} = 1.49\times10^{-10}\frac{L_{\rm TIR}}{L_\odot}. \quad (8)$$

We report the $L_{[\rm CII]}$, $\rm EW_{[CII]}$ and $\rm SFR_{[C\,II]}$ values obtained for the RL quasars in this work in Table 5. The $L_{\rm FIR}$, $M_{\rm dust}$, and $\rm SFR_{IR}$ for the RL quasars reported here were calculated considering the two flux density sets as described in Sect. 4.3. These values are listed in Table 7.

In Fig. 7, we show the distribution of $L_{[\rm CII]}$, $\rm EW_{[CII]}$, $\rm FWHM_{[CII]}$ and $\rm SFR_{[C\,II]}$, and their comparison with the literature sample of RQ and RL quasars. We also report the mean,

Table 5. [C II] luminosities, emission line equivalent widths, [C II] -based star formation rates, and the dynamical and [C II] -based molecular gas masses values for the RL quasars in our sample.

Name	$L_{[CII]}$ $[10^8\,L_\odot]$	$EW_{[CII]}$ $[km\,s^{-1}]$	$SFR_{[CII]}$ $[M_\odot\,yr^{-1}]$	M_{dyn} $[10^{10}\,M_\odot]$	$M_{H2,[C\,II]}$ $[10^9\,M_\odot]$
J0131-0321	3.8 ± 0.8	225 ± 45	40 ± 9	4.8 ± 4.0	11 ± 2.0
PSO055-00 (⋆)	3.1 ± 0.3	578 ± 78	32 ± 3	2.8 ± 2.2	9.3 ± 0.8
PSO135+16	27.7 ± 1.0	683 ± 35	416 ± 18	15.0 ± 1.8	83 ± 3.0
J1034+2033	3.1 ± 0.3	2476 ± 505	32 ± 4	5.8 ± 4.9	9.3 ± 0.9
PSO352–15	7.9 ± 1.1	2790 ± 472	95 ± 15	23.3 ± 10.7	24 ± 3.0

Notes. (⋆)We note that PSO055-00's line emission is recovered at the edge of the bandwith. Therefore, caution should be taken when considering its [C II] emission line value and all derived quantities.

median, and standard deviation of the two samples in Table 6. Despite the limited data for RL quasars with respect to the RQ ones, we can already note that the distribution of [C II] emission line EW and FWHM are similar between the two samples. We performed a Kolmogorov-Smirnov (KS) test to assess whether these properties are taken from the same underlying distribution and we report the corresponding p-values in Table 6. For p-values of <0.05, we can reject the null hypothesis (i.e., reject that the underlying distribution is the same). In our case, we calculated a p-value of 0.24 and 0.14 for EW and FWHM distributions, respectively, indicating that there are no systematic differences between RL and RQ quasars. Finally, we can observe potential differences in the distribution of [C II] emission line luminosities, where RL quasars seem to be systematically fainter than the RQ ones. We obtain a p-value of 0.04, moderately suggesting that there are differences in the two samples. More observations of [C II] emission in a larger sample of RL quasars at high-redshift will allow us to explore this hypothesis further.

An important effect observed in a variety of galaxies and active galactic nuclei (AGN) at high and low redshift is the so-called "[C II] deficit," which is a decrease in the $L_{[C\,II]}/L_{FIR}$ ratio as a function of IR luminosity. A unique understanding of the origin of this effect is still lacking, as there are several factors that could contribute to the suppression of [C II] luminosity. Some scenarios considered in the literature include: the ionization of C^+ due to X-ray radiation from an AGN, which would also boost FIR luminosities (e.g., Langer & Pineda 2015); self-absorption of [C II] in high density environments, which becomes higher than the critical density for collisional interaction (e.g., Díaz-Santos et al. 2017, Sutter et al. 2021); or the thermal saturation of C^+ due to strong far-UV radiation (e.g., Rybak et al. 2019). In Fig. 8, we show $L_{[C\,II]}/L_{FIR}$ versus L_{FIR} for different samples: star-forming galaxies and luminous IR galaxies (LIRGs) at $z < 1$ (Farrah et al. 2013, Sargsyan et al. 2014, Malhotra et al. 2001 and Díaz-Santos et al. 2013), star forming galaxies at $1 < z < 5$ (Stacey et al. 2010, Brisbin et al. 2015, Gullberg et al. 2015), and RQ and RL quasars at $z > 5$. In the low-redshift Universe, there is a clear decrement of [C II] luminosity with increasing FIR luminosity, while for high−z star forming galaxies, the scatter is larger. RQ quasars hosts at $z > 5$ follow a trend similar to low−z ULIRGs/star forming galaxies, with $L_{[C\,II]}/L_{FIR}$ between $\sim 10^{-2}$–10^{-3}. The RL quasar hosts mainly follow the distribution of RQ ones, with no strong dependency on the radio loudness parameter. We note that if we assume the entire ∼1 mm flux density as being due to dust, the quasars J0131-0321 and J0410-139 show the largest difference to the parameter space occupied by high−z quasars, with $L_{[C\,II]}/L_{FIR}$ ratios as low as 2.5–1.2×10^{-4}. However, if we consider the synchrotron contribution, these sources move closer to the locus of RQ quasar hosts.

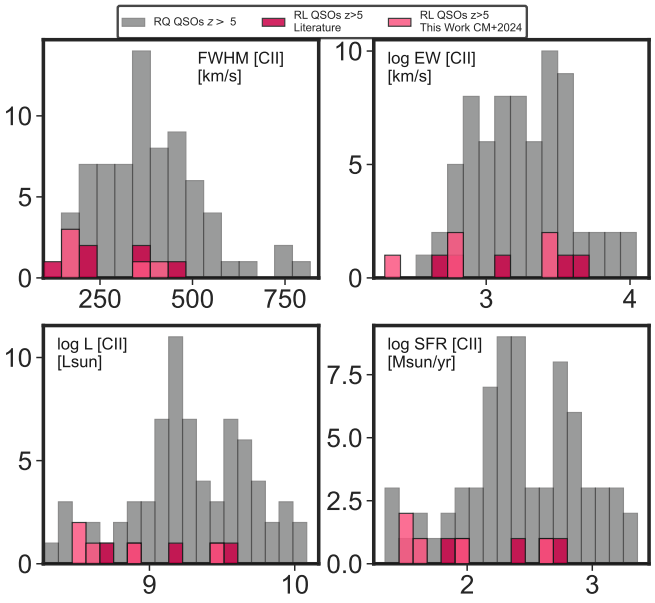

Fig. 7. Distribution of [C II] emission line and properties for RL (pink), and RQ (grey) quasars.

4.5. IR and CO(6-5) luminosities limits

We estimated the limits on the CO(6-5) emission line luminosities ($L_{CO(6-5)}$) using Eq. (1). We can also express the line luminosity via the quantity L' in units of [K km s^{-1} pc^2], following Carilli & Walter (2013) as

$$L'_{CO(6-5)} = 3.25{\times}10^7 {\times} \frac{F_{CO(6-5)}}{\mathrm{Jy\,km\,s^{-1}}} \frac{1}{(1+z)^3} \left(\frac{\nu_{obs}}{\mathrm{GHz}}\right)^{-2} \left(\frac{D_L}{\mathrm{Mpc}}\right)^2. \quad (9)$$

Additionally, we can estimate the limits on the FIR and total-IR luminosities, as done for the objects observed in Band 7 (see Sect. 3.1). All the limits on CO(6-5) and IR luminosities from Band 3 observations are reported in Table 3.

We compare the upper limits found here with CO(6-5) emission line observations in a sample of RQ quasars at $z > 5$ from the literature (Wang et al. 2010, 2013, 2019, Feruglio et al. 2018, 2023, Yang et al. 2019b, Decarli et al. 2022, Kaasinen et al. 2024). We also consider the source PSO352-15, part of the sample here. This source was observed with NOEMA at 101 GHz by Rojas-Ruiz et al. (2021). They estimated a 3σ limit on the CO(6-5) emission line of $L'_{CO(6-5)} < 5 \times 10^{10}$ K km s^{-1} pc^2 (see their

Table 6. Mean, median and standard deviation of the [C II] emission line properties shown in Fig. 7, for the RQ and RL high−z quasars samples.

	RQ quasars			RL quasars $^{(\star)}$			KS-test
	Mean	Median	st.dev	Mean	Median	st.dev	p-value
$FWHM_{[CII]}$ [km s^{-1}]	387	379	133	272	290	110	0.14
$EW_{[CII]}$ [km s^{-1}]	2362	1691	2013	1848	1180	1441	0.24
$L_{[CII]}$ [10^9 $L_\odot$]	2.9	1.8	2.6	1.5	0.8	1.2	0.04
$SFR_{[CII]}$ [$M_\odot$ yr^{-1}]	466	258	498	211	95	194	0.04

Notes. We also report the p-values obtained with a Kolmogorov-Smirnov test, to assess if the observed quantities for RQ and RL quasars were obtained from the same underlying distribution. $^{(\star)}$We only consider sources with [C II] emission lines detection, i.e., we excluded PSO172+18 from this comparison.

Sect. 3.2 for further details). Conversely, we consider the corresponding FIR luminosity derived in this work (see Table 7), which is consistent with the value reported by Rojas-Ruiz et al. (2021). We report L_{FIR}, re-calculated for the RQ sources in the literature with the method reported in Sect. 4.4 for consistency, as a function of CO(6-5) emission line luminosities in Fig. 9. We also report the expected relation between these two quantities calculated in Kamenetzky et al. (2016). The limits on these quantities for the two objects newly presented here do not show a critical difference between them and the RQ quasars sample. Given the somewhat loose constraints on the CO(6-5) luminosity of PSO352-15, this source is also consistent with the RQ quasars measurements. Deeper observations on a larger sample of RL quasars are needed to place more meaningful constraints.

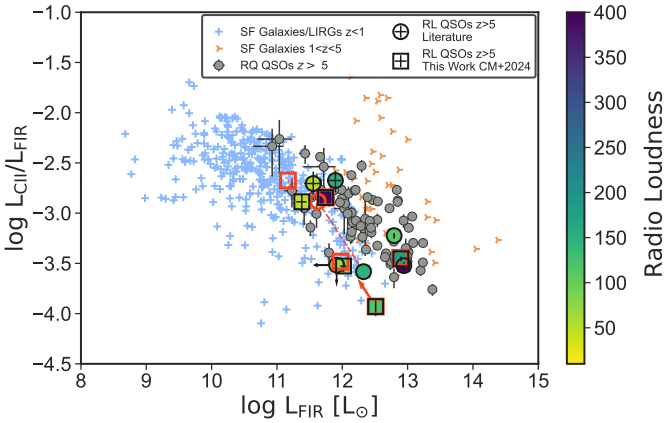

Fig. 8. [C II]-to-FIR luminosity ratio as a function of FIR luminosity. Observations of star-forming galaxies and LIRGs at $z < 1$ are shown with light blue crosses. We report the star-forming galaxies at $1 < z < 5$ with orange arrows. RQ quasars from the literature are depicted with grey points. All references for these data are reported in Sects. 4.1 and 4.4. The circles indicate the RL quasars observations from Khusanova et al. (2022), Venemans et al. (2020), and Banados et al. (2024b). The squares indicate the values derived in this work, assuming that the total measured ALMA continuum flux is due only to dust, all color-coded for radio loudness parameter. We note that RL quasars occupy a similar parameter space of that of RQ quasar hosts, with the exception of the sources J0131-0321 and J0410-0139 (with $L_{[C II]}/L_{FIR} \sim 10^{-3.5-4}$). When considering FIR luminosities accounting for the synchrotron contribution-derived flux (red squares for sources from this work, red circle from Banados et al. 2024b), even the above mentioned outliers move closer to the locations of the RQ quasar hosts.

4.6. Mass budget

A key physical parameter that one can derive from submm observations of high−z quasar hosts is the dynamical mass of the system. In combination with measurements of the central SMBH mass, this allows for studies of the SMBH and galaxy co-evolution at very high redshifts. Based on such comparisons, several works have shown that SMBHs in the EOR seem to be overmassive with respect to systems in the Local Universe (e.g., Farina et al. 2022; see Pacucci & Loeb 2024 for a recent compilation, but also Izumi et al. 2021).

In this work, the FIR continuum and [C II] emission of the radio-loud quasar host galaxies are unresolved (see Figs. 2 and A.1 and Table 4). Hence, the quality of our data prevents us from performing a full modeling of the kinematics of our sources, as done in studies of $z > 5$ quasar hosts with higher spatial resolution and S/N observations (e.g., Pensabene et al. 2020, Neeleman et al. 2021). Therefore, we estimate the dynamical masses of the host galaxies presented here in a simplified way, following Decarli et al. (2018). Briefly, under the assumption that the system is dominated by dispersion, we can express M_{dyn} with the following

$$M_{dyn} = \frac{3}{2}\frac{R_{[C II]}\sigma^2_{[C II]}}{G} = \frac{R_{[C II]}}{G}\left(\frac{0.75 FWHM_{[C II]}}{\sin(i)}\right)^2, \quad (10)$$

where $R_{[C II]}$ is the size of the [C II] emission line, considered as the major axis of the 2D Gaussian fit of the [C II] map, G is the gravitational constant, and $\sigma_{[C II]}$ is derived from the Gaussian fit of the line, which is equivalent to $0.75 \times FWHM_{[C II]}$. The second equation stands valid assuming that the width of the line is rotation-dominated, considering a flat disk structure with an inclination angle i. We utilized an angle of $i = 46°$; namely, the median inclination of a $z > 6$ quasar host sample derived by Wang et al. (2024a). We obtain dynamical masses between $2-20 \times 10^{10}$ $M_\odot$ (see Table 5). This is broadly consistent with values similarly obtained for RQ quasars in the literature (e.g., Decarli et al. 2018, Wang et al. 2024a).

We can also infer molecular masses (M_{H2}) relying on the [C II] luminosity, as calibrated from a sample of $z \sim 2$ main sequence and starburst galaxies by Zanella et al. (2018):

$$\frac{M_{H2,[C II]}}{M_\odot} = \frac{\alpha_{[C II]}}{M_\odot L_\odot^{-1}}\frac{L_{[C II]}}{L_\odot}, \quad (11)$$

with $\alpha_{[C II]} = 30\, M_\odot\, L_\odot^{-1}$. We report the values of $M_{H2,[C II]}$ for the sources presented here in Table 5. RL sources do not show significant differences with respect to RQ ones (e.g., Decarli et al. 2022).

Table 7. FIR luminosities, FIR-based star formation rates and dust masses for the RL quasars in our sample, calculated considering the total measured ALMA flux density (*tot*) and by correcting for the extrapolated synchrotron flux (*syn*).

Name	$L_{\rm FIR,tot}$ $[10^{11}\,L_\odot]$	$L_{\rm FIR,syn}$ $[10^{11}\,L_\odot]$	$\rm SFR_{IR,tot}$ $[M_\odot\,yr^{-1}]$	$\rm SFR_{IR,syn}$ $[M_\odot\,yr^{-1}]$	$M_{\rm dust,tot}$ $[10^7\,M_\odot]$	$M_{\rm dust,syn}$ $[10^7\,M_\odot]$
J0131-0321 (†)	32.4 ± 0.85	–	400 ± 10	–	19.9 ± 0.3	–
PSO055-00	10.5 ± 1.1	9.4 ± 1.1	129 ± 14	116 ± 14	2.8 ± 2.2	3.8 ± 0.4
PSO135+16	78.8 ± 2.9	77 ± 2.8	973 ± 35	951 ± 35	31.5 ± 1.1	30.7 ± 1.1
J1034+2033	2.4 ± 0.4	1.47 ± 0.4	30 ± 5	18 ± 5	0.9 ± 0.2	0.6 ± 0.2
PSO352–15	5.5 ± 0.6	5.5 ± 0.8	68 ± 7	68 ± 7	2.2 ± 0.2	2.2 ± 0.2

Notes. (†)The synchrotron contribution could amount to almost all the flux density at ∼300 GHz for this source. Hence, we report in this case only the IR values obtained from considering the total measured ALMA flux density as due to the dust, and use them as upper limits.

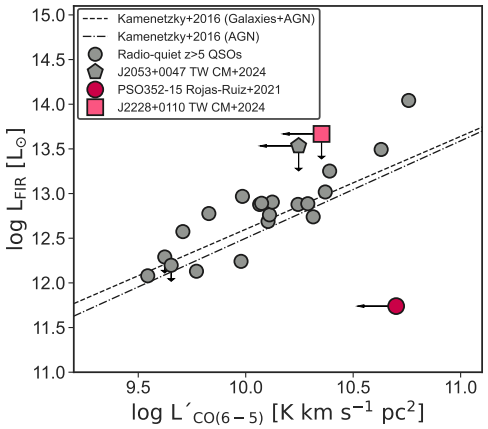

Fig. 9. FIR (42–122.5 µm) luminosity vs. CO(6-5) luminosity for the two sources observed in Band 3 in our sample (J2053+0047, RQ, grey penthagon; J2228+0110, RL, pink square), compared to a sample of RQ $z > 5$ quasars in the literature (grey circles; see text for references). Measurements and limits for the RL quasar PSO352-15 are also shown (Rojas-Ruiz et al. 2021; dark pink circle). The relations measured for galaxies + AGN, and only AGN, at lower−z, in Kamenetzky et al. (2016) are also reported (dashed and dot-dashed black lines). The sources in this work are consistent with values in the literature, particularly given the relatively loose limits on both the IR and CO(6-5) emission line luminosities.

4.7. Impact of AGN luminosity on [C II] and FIR emission

Unveiling the relative role of AGN versus star formation in heating gas and dust in the ISM is crucial to our understanding of quasar and galaxy (co)evolution, especially at high redshift. A useful approach relies on comparisons of observations of different FIR emission lines (e.g., [N II] 205 µm, [O I] 146 µm, [O III] 88 µm, and [C I] 369 µm) with the output of photoionization codes (e.g., CLOUDY; Ferland et al. 2017). Some works in the literature provide these studies for few $z \gtrsim 6$ quasars, showing that their host galaxies are mainly heated by star formation, with apparently no evident contribution from the AGN (e.g., Venemans et al. 2017b, Novak et al. 2019, Pensabene et al. 2021, Meyer et al. 2022a).

However, such investigations are currently limited to a few objects, due to the time consuming nature of the observations of different, faint lines in the (sub)mm. Hence, to gauge the AGN contribution to the host galaxy in a larger sample of quasars, we can resort to more straightforward methods; for instance, by comparing the absolute UV magnitude at a rest frame wavelength of 1450 Å, linked with the AGN activity, to the FIR and [C II] luminosities (arising instead from the host galaxy). Decarli et al. (2018) and Venemans et al. (2018) provided this comparison for ∼30 UV-bright quasars observed with ALMA, remarking that no strong correlation between UV and FIR was recovered, especially when focusing on the more complete sample at high UV luminosities. Venemans et al. (2020) confirmed this lack of correlation with ALMA observations at higher (∼kpc) spatial resolution, concluding that not even the most central FIR emission seemed to be affected by the presence of an AGN.

Here, we show $L_{\rm [C\,II]}$ and $L_{\rm FIR}$ as a function of M_{1450} for the RQ quasars sample from the literature and for the RL quasars (Fig. 10). We note that the majority of the RL quasars fall in the same parameter space as the RQ ones, that is, in both samples, when considering a given UV luminosity, we observe a large range of $L_{\rm [C\,II]}$ and $L_{\rm FIR}$ values; here, we also see a scatter larger than an order of magnitude. No strong correlation with radio-loudness can be recovered. However, we note that a few objects (J0131-0321, J1034+2033, PSO055-00, and PSO172+18) are outliers in the $L_{\rm [C\,II]}$ vs. M_{1450} plane; namely, they show a much lower [C II] luminosity than that observed in RQ quasars with a comparable UV luminosity.

4.8. Companions

RL quasars and radio galaxies are found to be surrounded by overdensities of galaxies (e.g., Wylezalek et al. 2013, Gilli et al. 2019). Different studies using rest-frame UV observations have uncovered a rich environment around the $z \sim 5.8$ RL quasar J0836+0054 (e.g., Zheng et al. 2006, Ajiki et al. 2006, Bosman et al. 2020, Overzier 2022). At the same time, ALMA observations of RQ quasars found several line-emitters in their surroundings, from systems in advanced mergers to galaxies at tens of kpc distances (e.g., Decarli et al. 2017, Trakhtenbrot et al. 2017, Nguyen et al. 2020, Neeleman et al. 2021). Nevertheless, we note that studies looking for continuum dust emitters around quasars were not successful in discovering clear overdensities (e.g., Champagne et al. 2018, Meyer et al. 2022b).

In this work, we search for line emitters in the fields of the RL quasars observed in Band 7, using the continuum emission subtracted cubes, obtained as described in Sect. 3.1. We utilized the code *findclumps*[4] (Walter et al. 2016). In brief, *findclumps* performs a floating average of channels over different spectral windows. For each window, it searches for positive and negative emission peaks at different S/N, where the noise is calculated as

[4] With the python implementation provided in the interferopy package: https://interferopy.readthedocs.io/en/latest/index.html, Boogaard & Meyer (2021).

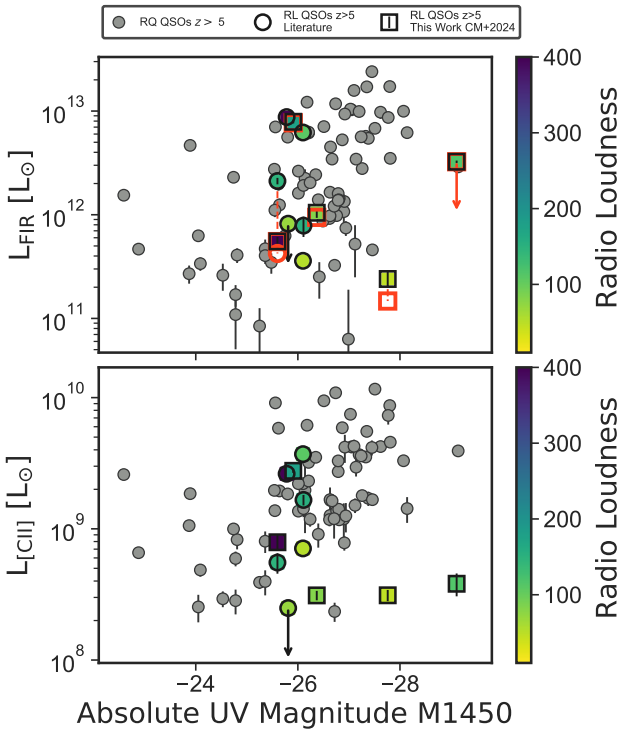

Fig. 10. FIR (top) and [C II] (bottom) luminosity vs. absolute UV magnitude at a rest-frame wavelength of 1450 Å. RQ quasars from the literature (see Sect. 4.1 for references) and RL quasars are shown with the same symbols as in Fig. 8.

the rms of the collapsed map. In this work, we use spectral windows of width between 3 and 19 channels. We cropped multiple entries by discarding sources which are closer than 2″. Finally, we perform a fidelity check to test the reliability of our candidates. Under the assumption that the positive emission comprehends real astrophysical sources and noise, while the negative emission are due only to noise, we use the following equation (Walter et al. 2016):

$$\text{fidelity(S/N)} = 1 - \frac{N_{\text{neg}}(\text{S/N})}{N_{\text{pos}}(\text{S/N})} \quad (12)$$

with N_{neg}(S/N) and N_{pos}(S/N) are the number of negative and positive detections at a certain S/N, respectively. In order to not be limited by the low number counts of positive and negative detections around each quasar, we compute the fidelity considering the catalogs obtained from of all the quasars fields at once. Following Venemans et al. (2020) and Meyer et al. (2022b), we assumed a fidelity threshold as calculated in each channel of 90% (Fidelity > 0.9). We selected sources with S/N > 4, although it is worthwhile to notice that the cut on fidelity already selects sources with S/N $\gtrsim$ 4–5. We cropped sources close to the edge of the field of view and those at a distance of $\Delta v > \pm 1000\,\text{km s}^{-1}$[5] (e.g., Venemans et al. 2020).

Considering all the above conditions, we did not recover any companion candidate in our RL quasars fields. We can still compare this result with what observed around RQ quasars fields and with the expectations from blank fields. In particular, Venemans et al. (2020) found 27 line emitters in the fields of 14 RQ quasars at $z \sim 6$, out of 26 fields inspected. Of these sources, 19 (17) were identified as [C II] emitters companion candidates to the quasars, with $\Delta v < 2000\,\text{km s}^{-1}$ ($\Delta v < 1000\,\text{km s}^{-1}$). They also discovered three companion candidates in the field of the RL quasar J2318-3113. However, the studies in our work and that of Venemans et al. (2020) are characterized by different depths. If we consider solely the companion candidates around RQ quasars that would satisfy our S/N > 4 criterion, for a [C II] emission line with typical FWHM ~ 300 km s^{-1} ($F_{[\text{C II}]} \sim 1.77\,\text{Jy km s}^{-1}$), we are left with only three sources. These sources (in the fields of J0842+1218, PSO231-20, and J2100-1715) were also recovered by Decarli et al. (2017), whose observations sensitivity is similar to that of our work. We also note that the companion candidates found by Venemans et al. (2020) around J2338-3113 are fainter than the detection limits of our observations. Hence, at the depth of our work, one would expect to recover 3 [C II] emitting companion candidates in 26 RQ quasars fields, namely, in only ~10% of the fields. This is still consistent with finding zero companion candidates in five fields. We can also compare our results with the expected number of sources in a blank field, that is, with no quasar. We consider the number density of [C II] emitting sources provided in Uzgil et al. (2021) and Decarli et al. (2020), in the redshift range $z = 6$–8, with $L_{[\text{C II}]} > 2.8 \times 10^8\,L_\odot$[6] ($<1.94 \times 10^{-4}\,\text{Mpc}^{-3}$; see Table 3 in Uzgil et al. 2021). Considering the total volume covered in the 5 RL quasars fields observed here, within $\Delta v < 1000\,\text{km s}^{-1}$, we would expect to observe <0.02 sources.

In conclusion, given the depth of our current observations and the number of fields explored, we are not able to place strong constraints on the properties of the fields of RL quasars. More specifically, we find that they are still consistent with both the expectations of blank fields and RQ quasars fields. Larger samples of RL quasars targeted in the submm and/or with deeper observations will allow for further comparisons between the two samples to make progress in this area of research.

5. Discussion

The interaction between radio jets and the ISM of galaxies is expected to produce different outcomes, depending on various circumstances local to each galaxy and their proximate environment. As seen in both observations and simulations, a radio jet can drive massive, multiphase (ionized, warm and molecular gas) outflows, whose geometry (following the jet direction, or perpendicular to it) depends on the jet inclination and jet-ISM coupling (e.g., Morganti et al. 2015, Meenakshi et al. 2022, Zhong et al. 2024). This mechanism will also boost the gas turbulence, thereby increasing the observed gas velocity and dispersion (e.g., Venturi et al. 2023). In addition, the passage of the jet can form density fluctuations in the ISM, forming hot (>150 K) and dense (>10^5 cm^{-3}) gas that can be observed via several CO emission lines, with an increase in the flux of higher J level transitions (e.g., Audibert et al. 2023). At the same time, observations of spectacular cases of RL AGN at low−z (e.g., Guillard et al. 2015, Appleton et al. 2018) showed how the [C II] emission line can originate from shocks and/or outflows and trace the radio jet-ISM interaction. Smirnova-Pinchukova et al. (2019) reported a significant boost of [C II] emission in a nearby AGN with radio jets, with a $L_{[\text{C II}]}/L_{\text{IR}}$ ratio ten times higher than other AGN at comparable redshifts. Considering all these, we might expect in RL quasars to observe [C II] emission lines with larger FWHM,

[5] We note that changing this limit to $\Delta v > \pm 2000\,\text{km s}^{-1}$ does not change our final results.

[6] We note that our data is shallower, by a factor of ~3, than those used to determine the blank field number density.

and/or asymmetric line profiles, or peculiar morphologies and with higher luminosities with respect to what was recovered in the RQ ones. On the contrary, the [C II] luminosities of the sources in our sample are comparable or slightly lower than those observed in $z \sim 6$ RQ quasars, and we did not recover any strong differences in FWHM values, spectral profiles or morphologies. This can be due to the fact that the aforementioned mechanisms might not be instantaneous or could only be important on local scales; hence, they have proven difficult to highlight with our integrated, spatially unresolved, and low S/N observations (see also Molyneux et al. 2024, for comparable conclusions in a study of a sample of $z < 0.2$ radio AGN). Moreover, high spatial-resolution observations highlight that several high−z RQ quasar hosts are found in mergers, which can broaden the apparent FWHM values (Neeleman et al. 2021), complicating the comparison. Another important aspect to consider is the possibility that extreme feedback from radio jets can displace the gas and remove it altogether from the gravitational influence of the galaxy (e.g., Murthy et al. 2022). The marginally lower [C II] luminosities observed in our high−z RL quasars sample may than be the result of such a process. Finally, however, it is important to notice that the complex physical mechanisms responsible for [C II] emission complicate the interpretation of our results. Higher S/N and angular resolution [C II] observations are necessary to disentangle these different interpretations.

Conversely, it is believed that radio-loud AGN are preferentially found in major mergers, which could trigger the nuclear accretion and the formation of the jets by funnelling a large amount of gas towards the center (e.g., Chiaberge et al. 2015, Breiding et al. 2024). At the same time, as discussed above, RL sources are expected to be found in overdensities of galaxies (e.g., Wylezalek et al. 2013, Hatch et al. 2014). Khusanova et al. (2022) showed potential evidence for a larger merger fraction amongst $z > 6$ RL quasars (>40%) with respect to RQ ones (∼30%; Neeleman et al. 2021). We did not recover merger signs in the RL quasars newly studied in this work. If we consider the entire sample of RL quasars (this work + literature), we recover only two sources that are potentially hosted in a major merger, allowing for a merger fraction of ∼20%, even lower than that observed in RQ quasars. At the same time, none of the RL quasars inspected is surrounded by strong overdensities of bright [C II] emitters. Given the course angular resolution and low S/N of our observations, and the limited sample reported, we have refrained from drawing further conclusions.

6. Conclusions and outlooks

In this work, we present new ALMA observations of six RL and one RQ quasars at $z > 5$. We acquired data in Band 7 (5 RL sources), targeting the [C II] emission line and underlying dust continuum, and in Band 3 (2 sources, 1 RL and 1 RQ), focusing on the CO(6-5) line. We detect (at σ >2) the [C II] emission line and continuum for the quasars targeted in Band 7 (Tables 2, 4). However, no emission was recovered in Band 3; hence, we can only place upper limits on the relative CO(6-5) emission line flux and luminosity, along with the underlying dust continuum and IR luminosity (Table 3).

At the current spatial resolution (∼1.″0−1.″4), no extended or disturbed morphologies are clearly detected in the Band 7 continuum maps (Figs. 4 and 5), nor in the continuum-subtracted [C II] emission line maps (Fig. 2). Specifically, the source sizes are broadly consistent with the beam sizes. All the extracted [C II] 1D spectra are well fitted with a single Gaussian function (Fig. 1). Hence, there is no strong evidence for mergers in the RL quasars hosts newly analyzed here.

Considering our new ALMA data and radio/submm observations from the literature, we built the SEDs of the six RL quasars studied here (Fig. 6). Although the observations forming the SEDs were obtained at different epochs and were not corrected for any potential variability, we observe that the ALMA 1 mm measurements are consistent with being a combination of the high-frequency tail of radio synchrotron emission and dust continuum emission. In at least four sources, this contribution is estimated to be >9%, and in two cases, J1034+2033 and J0131-0321, it can be as high as ∼40% and ∼100%, respectively. Hence, extreme caution should be taken when deriving the dust properties (luminosities, masses, SFR) for these objects. Given the limited data at hands, a full spectral fit of the different components is currently beyond of the scope of this work.

We derived estimates on the [C II] and IR luminosities, as well as on the dust, dynamical, and molecular gas masses, as well as the [C II]- and IR-based SFRs considering two scenarios. First, under the assumption that all the continuum emission arises from the galaxies' ISM and second, by accounting for our initial estimate of the synchrotron contribution (see Sects. 4.4 and 4.6). The hosts of the RL quasars observed in this work present relatively large cool gas reservoirs, with $L_{[C\,II]} \sim 3-30 \times 10^8$, $M_{dyn} \sim 1-10 \times 10^{10}\,M_\odot$, and $M_{H2,[C\,II]} \sim 9-80 \times 10^9\,M_\odot$. Moreover, they are also actively forming stars, with $SFR_{[C\,II]} \sim 30-400\,M_\odot\,yr^{-1}$.

We placed these new measurements in the context of observations of RQ and RL quasar hosts from the literature. The [C II] EW and FWHM in RL quasars are broadly consistent with those of RQ ones, but we observe slightly lower [C II] luminosities and SFR for RL sources (with a p-value of ∼0.04; Fig. 7 and Table 6). Furthermore, the [C II] decrement in RL quasar hosts is in the same parameter space as those of RQ ones, with no dependency on radio loudness parameter. When considering the synchrotron contribution at ∼1 mm, even outlier cases (e.g., J0131-0321 and J0410-0139) are consistent with RQ quasars (Fig. 8).

Additionally, we search for line emitting candidates in the fields of the five RL quasars observed in Band 7 in this work, using the *findclumps* code, and selecting sources with a fidelity value higher than 0.9, a S/N > 4, excluding the edges of the images, and within $\Delta v < 1000\,km\,s^{-1}$ (see Sect. 4.8). We did not recover any [C II] emitting companion candidate. Comparing this result with the number of sources expected in a blank field and observed around a sample of RQ quasars at $z \sim 6$, we see that the fields of RL quasars are still comparable with RQ ones or the blank field, given the depth of our data.

Several approaches will be important for further investigations of high−z RL quasar hosts properties. In the recent years, the number of RL quasars at high−z has strongly increased (e.g., Gloudemans et al. 2022, Belladitta et al. 2023), allowing for the coverage of a larger sample of such sources in the future. This will facilitate a more meaningful comparison with RQ quasar hosts. In addition, radio/submm observations of RL quasars over a large frequency range, covering the spectral region dominated by the jet and down to the peak of the modified black body dust emission with several facilities (i.e., ALMA, VLA, NOEMA, and uGMRT) will allow for a full fit of the SEDs. Hence, it will be possible to properly disentangle the non-thermal synchrotron and dust contributions and to place strong constraints on the ISM properties of the host galaxies. Moreover, follow-up observations of different submm emission lines (e.g., [N II] 205 μm, [O I] 146 μm, [O III] 88 μm, [C I] 369 μm, high-J CO transitions) would enable constraints on the role of the

central AGN and/or of the radio jets in the arising of the [C II] and continuum emission (e.g., Pensabene et al. 2021, Li et al. 2024). Additional higher spatial-resolution and S/N data targeted at the [C II] emission line could allow for constraints to be placed on more complex morphological and kinematic signatures, which might be due to merger events or the passage of a radio jet (e.g., Neeleman et al. 2021, Khusanova et al. 2022). The recently launched JWST has already demonstrated the key role it serves in unveiling the properties of the hot ionized gas in both high-redshift quasar hosts and galaxies (e.g., Ding et al. 2023, Marshall et al. 2023) and in powerful jetted and non-jetted AGN at cosmic noon (e.g., Wylezalek et al. 2022, Cresci et al. 2023, Vayner et al. 2023, Wang et al. 2024b). Thus, deep NIRSpec IFU/NIRCAM observations of $z > 5$ RL quasar hosts would shed a fundamental light on the rest-frame optical properties of such galaxies; for instance, the underlying stellar continuum emission, black hole mass, and accretion rate from the Hα or Hβ emission line modeling, any central or extended outflow via observations of the [OIII] emission lines, and the characterization of the warm ionized ISM. Such studies would help to uncover any existing interplay with the radio jets and their role in launching complex, multi-phase outflows.

Acknowledgements. We thank the anonymous referee, who's feedback greatly improved the paper. This paper makes use of the following ALMA data: ADS/JAO.ALMA#2019.1.00840.S. ALMA is a partnership of ESO (representing its member states), NFS (USA) and NINS (Japan), together with NRC (Canada), MOST and ASIAA (Taiwan) and KASI (Republic of Korea), in cooperation with the Republic of Chile. The Joint ALMA Observatory is operated by ESO, AUI/NRAO and NAOJ. This scientific work uses data obtained from Inyarrimanha Ilgari Bundara / the Murchison Radio-astronomy Observatory. We acknowledge the Wajarri Yamaji People as the Traditional Owners and native title holders of the Observatory site. CSIRO's ASKAP radio telescope is part of the Australia Telescope National Facility (https://ror.org/05qajvd42). Operation of ASKAP is funded by the Australian Government with support from the National Collaborative Research Infrastructure Strategy. ASKAP uses the resources of the Pawsey Supercomputing Research Centre. Establishment of ASKAP, Inyarrimanha Ilgari Bundara, the CSIRO Murchison Radio-astronomy Observatory and the Pawsey Supercomputing Research Centre are initiatives of the Australian Government, with support from the Government of Western Australia and the Science and Industry Endowment Fund. This paper includes archived data obtained through the CSIRO ASKAP Science Data Archive, CASDA (https://data.csiro.au). The National Radio Astronomy Observatory is a facility of the National Science Foundation operated under cooperative agreement by Associated Universities, Inc. C.M. acknowledges support from Fondecyt Iniciacion grant 11240336 and the ANID BASAL project FB210003. F.W. acknowledges support from the US NSF Grant AST-2308258. R.A.M acknowledges support from the Swiss National Science Foundation (SNSF) through project grant 200020_207349.

References

Ajiki, M., Taniguchi, Y., Murayama, T., et al. 2006, PASJ, 58, 499
Allison, J. R., Sadler, E. M., Amaral, A. D., et al. 2022, PASA, 39, e010
Appleton, P. N., Diaz-Santos, T., Fadda, D., et al. 2018, ApJ, 869, 61
Audibert, A., Ramos Almeida, C., García-Burillo, S., et al. 2023, A&A, 671, L12
Bañados, E., Decarli, R., Walter, F., et al. 2015a, ApJ, 805, L8
Bañados, E., Venemans, B. P., Morganson, E., et al. 2015b, ApJ, 804, 118
Bañados, E., Venemans, B. P., Decarli, R., et al. 2016, ApJS, 227, 11
Bañados, E., Venemans, B. P., Mazzucchelli, C., et al. 2018a, Nature, 553, 473
Bañados, E., Carilli, C., Walter, F., et al. 2018b, ApJ, 861, L14
Bañados, E., Mazzucchelli, C., Momjian, E., et al. 2021, ApJ, 909, 80
Bañados, E., Schindler, J.-T., Venemans, B. P., et al. 2023, ApJS, 265, 29
Banados, E., Momjian, E., Connor, T., et al. 2024a, arXiv e-prints [arXiv:2407.07236]
Banados, E., Khusanova, Y., Decarli, R., et al. 2024b, arXiv e-prints [arXiv:2408.12299]
Becker, R. H., White, R. L., & Helfand, D. J. 1995, ApJ, 450, 559
Beelen, A., Cox, P., Benford, D. J., et al. 2006, ApJ, 642, 694
Belladitta, S., Moretti, A., Caccianiga, A., et al. 2019, A&A, 629, A68
Belladitta, S., Moretti, A., Caccianiga, A., et al. 2020, A&A, 635, L7
Belladitta, S., Moretti, A., Caccianiga, A., et al. 2023, A&A, 669, A134
Bischetti, M., Maiolino, R., Carniani, S., et al. 2019, A&A, 630, A59
Boogaard, L., & Meyer, R. A. 2021, https://doi.org/10.5281/zenodo.5775603
Bosman, S. E. I., Kakiichi, K., Meyer, R. A., et al. 2020, ApJ, 896, 49
Breiding, P., Chiaberge, M., Lambrides, E., et al. 2024, ApJ, 963, 91
Brisbin, D., Ferkinhoff, C., Nikola, T., et al. 2015, ApJ, 799, 13
Carilli, C. L., & Walter, F. 2013, ARA&A, 51, 105
Champagne, J. B., Decarli, R., Casey, C. M., et al. 2018, ApJ, 867, 153
Chiaberge, M., Gilli, R., Lotz, J. M., & Norman, C. 2015, ApJ, 806, 147
Cresci, G., Tozzi, G., Perna, M., et al. 2023, A&A, 672, A128
da Cunha, E., Groves, B., Walter, F., et al. 2013, ApJ, 766, 13
Decarli, R., Walter, F., Yang, Y., et al. 2012, ApJ, 756, 150
Decarli, R., Walter, F., Venemans, B. P., et al. 2017, Nature, 545, 457
Decarli, R., Walter, F., Venemans, B. P., et al. 2018, ApJ, 854, 97
Decarli, R., Aravena, M., Boogaard, L., et al. 2020, ApJ, 902, 110
Decarli, R., Pensabene, A., Venemans, B., et al. 2022, A&A, 662, A60
De Looze, I., Baes, M., Bendo, G. J., Cortese, L., & Fritz, J. 2011, MNRAS, 416, 2712
De Looze, I., Cormier, D., Lebouteiller, V., et al. 2014, A&A, 568, A62
Díaz-Santos, T., Armus, L., Charmandaris, V., et al. 2013, ApJ, 774, 68
Díaz-Santos, T., Armus, L., Charmandaris, V., et al. 2017, ApJ, 846, 32
Ding, X., Onoue, M., Silverman, J. D., et al. 2023, Nature, 621, 51
Drake, A. B., Farina, E. P., Neeleman, M., et al. 2019, ApJ, 881, 131
Dunne, L., Eales, S., Edmunds, M., et al. 2000, MNRAS, 315, 115
Eilers, A.-C., Hennawi, J. F., Decarli, R., et al. 2020, ApJ, 900, 37
Eilers, A.-C., Hennawi, J. F., Decarli, R., et al. 2021, ApJ, 914, 74
Fan, X., Narayanan, V. K., Lupton, R. H., et al. 2001, AJ, 122, 2833
Fan, X., Strauss, M. A., Becker, R. H., et al. 2006, AJ, 132, 117
Fan, X., Bañados, E., & Simcoe, R. A. 2023, ARA&A, 61, 373
Farina, E. P., Arrigoni-Battaia, F., Costa, T., et al. 2019, ApJ, 887, 196
Farina, E. P., Schindler, J.-T., Walter, F., et al. 2022, ApJ, 941, 106
Farrah, D., Lebouteiller, V., Spoon, H. W. W., et al. 2013, ApJ, 776, 38
Ferland, G. J., Chatzikos, M., Guzmán, F., et al. 2017, Rev. Mex. Astron. Astrofis., 53, 385
Feruglio, C., Fiore, F., Carniani, S., et al. 2018, A&A, 619, A39
Feruglio, C., Maio, U., Tripodi, R., et al. 2023, ApJ, 954, L10
Fragile, P. C., Anninos, P., Croft, S., Lacy, M., & Witry, J. W. L. 2017, ApJ, 850, 171
Gabanyi, K. E., Cseh, D., Frey, S., et al. 2015, MNRAS, 450, L57
Ghisellini, G., Tagliaferri, G., Sbarrato, T., & Gehrels, N. 2015, MNRAS, 450, L34
Gilli, R., Mignoli, M., Peca, A., et al. 2019, A&A, 632, A26
Gloudemans, A. J., Duncan, K. J., Saxena, A., et al. 2022, A&A, 668, A27
Guillard, P., Boulanger, F., Lehnert, M. D., et al. 2015, A&A, 574, A32
Gullberg, B., De Breuck, C., Vieira, J. D., et al. 2015, MNRAS, 449, 2883
Hale, C. L., McConnell, D., Thomson, A. J. M., et al. 2021, PASA, 38, e058
Hatch, N. A., Wylezalek, D., Kurk, J. D., et al. 2014, MNRAS, 445, 280
Helou, G., Khan, I. R., Malek, L., & Boehmer, L. 1988, ApJS, 68, 151
Herrera-Camus, R., Bolatto, A. D., Wolfire, M. G., et al. 2015, ApJ, 800, 1
Ighina, L., Belladitta, S., Caccianiga, A., et al. 2021, A&A, 647, L11
Ighina, L., Caccianiga, A., Moretti, A., et al. 2024, A&A, 687, A242
Intema, H. T., Jagannathan, P., Mooley, K. P., & Frail, D. A. 2017, A&A, 598, A78
Izumi, T., Onoue, M., Shirakata, H., et al. 2018, PASJ, 70, 36
Izumi, T., Onoue, M., Matsuoka, Y., et al. 2019, PASJ, 71, 111
Izumi, T., Onoue, M., Matsuoka, Y., et al. 2021, ApJ, 908, 235
Jaffe, W. J., & Perola, G. C. 1973, A&A, 26, 423
Jiang, L., Fan, X., Ivezić, Ž., et al. 2007, ApJ, 656, 680
Jiang, L., Fan, X., Bian, F., et al. 2009, AJ, 138, 305
Kaasinen, M., Venemans, B., Harrington, K. C., et al. 2024, A&A, 684, A33
Kamenetzky, J., Rangwala, N., Glenn, J., Maloney, P. R., & Conley, A. 2016, ApJ, 829, 93
Kellermann, K. I., Sramek, R., Schmidt, M., Shaffer, D. B., & Green, R. 1989, AJ, 98, 1195
Kennicutt, R. C., & Evans, N. J. 2012, ARA&A, 50, 531
Khusanova, Y., Bañados, E., Mazzucchelli, C., et al. 2022, A&A, 664, A39
Krezinger, M., Baldini, G., Giroletti, M., et al. 2024, A&A, 690, A321
Lai, S., Bian, F., Onken, C. A., et al. 2022, MNRAS, 513, 1801
Langer, W. D., & Pineda, J. L. 2015, A&A, 580, A5
Li, J., Wang, R., Pensabene, A., et al. 2024, ApJ, 962, 119
Liu, Y., Wang, R., Momjian, E., et al. 2021, ApJ, 908, 124
Maiolino, R., Cox, P., Caselli, P., et al. 2005, A&A, 440, L51
Malhotra, S., Kaufman, M. J., Hollenbach, D., et al. 2001, ApJ, 561, 766
Marshall, M. A., Mechtley, M., Windhorst, R. A., et al. 2020, ApJ, 900, 21
Marshall, M. A., Perna, M., Willott, C. J., et al. 2023, A&A, 678, A191
Matsuoka, Y., Iwasawa, K., Onoue, M., et al. 2018, ApJS, 237, 5
Mazzucchelli, C., Bañados, E., Venemans, B. P., et al. 2017, ApJ, 849, 91

Mazzucchelli, C., Decarli, R., Farina, E. P., et al. 2019, ApJ, 881, 163
Mazzucchelli, C., Bischetti, M., D'Odorico, V., et al. 2023, A&A, 676, A71
McConnell, D., Hale, C. L., Lenc, E., et al. 2020, PASA, 37, e048
McMullin, J. P., Waters, B., Schiebel, D., Young, W., & Golap, K. 2007, ASP Conf. Ser., 376, 127
Mechtley, M., Windhorst, R. A., Ryan, R. E., et al. 2012, ApJ, 756, L38
Meenakshi, M., Mukherjee, D., Wagner, A. Y., et al. 2022, MNRAS, 516, 766
Meyer, R. A., Bosman, S. E. I., & Ellis, R. S. 2019, MNRAS, 487, 3305
Meyer, R. A., Walter, F., Cicone, C., et al. 2022a, ApJ, 927, 152
Meyer, R. A., Decarli, R., Walter, F., et al. 2022b, ApJ, 927, 141
Molyneux, S. J., Calistro Rivera, G., De Breuck, C., et al. 2024, MNRAS, 527, 4420
Momjian, E., Carilli, C. L., Bañados, E., Walter, F., & Venemans, B. P. 2018, ApJ, 861, 86
Momjian, E., Bañados, E., Carilli, C. L., Walter, F., & Mazzucchelli, C. 2021, AJ, 161, 207
Morganti, R., Oosterloo, T., Oonk, J. B. R., Frieswijk, W., & Tadhunter, C. 2015, A&A, 580, A1
Murthy, S., Morganti, R., Wagner, A. Y., et al. 2022, Nat. Astron., 6, 488
Neeleman, M., Novak, M., Venemans, B. P., et al. 2021, ApJ, 911, 141
Nguyen, N. H., Lira, P., Trakhtenbrot, B., et al. 2020, ApJ, 895, 74
Novak, M., Bañados, E., Decarli, R., et al. 2019, ApJ, 881, 63
Novak, M., Venemans, B. P., Walter, F., et al. 2020, ApJ, 904, 131
Onoue, M., Bañados, E., Mazzucchelli, C., et al. 2020, ApJ, 898, 105
Onoue, M., Ding, X., Silverman, J. D., et al. 2024, arXiv e-prints [arXiv:2409.07113]
Overzier, R. A. 2022, ApJ, 926, 114
Pacucci, F., & Loeb, A. 2024, ApJ, 964, 154
Pâris, I., Petitjean, P., Aubourg, É., et al. 2018, A&A, 613, A51
Pensabene, A., Carniani, S., Perna, M., et al. 2020, A&A, 637, A84
Pensabene, A., Decarli, R., Bañados, E., et al. 2021, A&A, 652, A66
Reed, S. L., Banerji, M., Becker, G. D., et al. 2019, MNRAS, 487, 1874
Roche, N., Humphrey, A., & Binette, L. 2014, MNRAS, 443, 3795
Rojas-Ruiz, S., Bañados, E., Neeleman, M., et al. 2021, ApJ, 920, 150
Rybak, M., Calistro Rivera, G., Hodge, J. A., et al. 2019, ApJ, 876, 112
Salomé, Q., Salomé, P., & Combes, F. 2015, A&A, 574, A34
Sargsyan, L., Lebouteiller, V., Weedman, D., et al. 2012, ApJ, 755, 171
Sargsyan, L., Samsonyan, A., Lebouteiller, V., et al. 2014, ApJ, 790, 15
Sbarrato, T., Ghisellini, G., Tagliaferri, G., et al. 2022, A&A, 663, A147
Schindler, J.-T., Farina, E. P., Bañados, E., et al. 2020, ApJ, 905, 51
Schneider, D. P., Richards, G. T., Hall, P. B., et al. 2010, AJ, 139, 2360
Shao, Y., Wagg, J., Wang, R., et al. 2020, A&A, 641, A85
Shao, Y., Wagg, J., Wang, R., et al. 2022, A&A, 659, A159
Silk, J. 2013, ApJ, 772, 112
Smirnova-Pinchukova, I., Husemann, B., Busch, G., et al. 2019, A&A, 626, L3
Stacey, G. J., Hailey-Dunsheath, S., Ferkinhoff, C., et al. 2010, ApJ, 724, 957
Stone, M. A., Lyu, J., Rieke, G. H., & Alberts, S. 2023, ApJ, 953, 180
Stone, M. A., Lyu, J., Rieke, G. H., Alberts, S., & Hainline, K. N. 2024, ApJ, 964, 90
Sutter, J., Dale, D. A., Sandstrom, K., et al. 2021, MNRAS, 503, 911
Trakhtenbrot, B., Lira, P., Netzer, H., et al. 2017, ApJ, 836, 8
Uzgil, B. D., Oesch, P. A., Walter, F., et al. 2021, ApJ, 912, 67
Vayner, A., Zakamska, N. L., Ishikawa, Y., et al. 2023, ApJ, 955, 92
Venemans, B. P., Röttgering, H. J. A., Miley, G. K., et al. 2007, A&A, 461, 823
Venemans, B. P., Walter, F., Zschaechner, L., et al. 2016, ApJ, 816, 37
Venemans, B. P., Walter, F., Decarli, R., et al. 2017a, ApJ, 851, L8
Venemans, B. P., Walter, F., Decarli, R., et al. 2017b, ApJ, 845, 154
Venemans, B. P., Decarli, R., Walter, F., et al. 2018, ApJ, 866, 159
Venemans, B. P., Walter, F., Neeleman, M., et al. 2020, ApJ, 904, 130
Venturi, G., Treister, E., Finlez, C., et al. 2023, A&A, 678, A127
Villar Martín, M., Emonts, B., Humphrey, A., Cabrera Lavers, A., & Binette, L. 2014, MNRAS, 440, 3202
Walter, F., Riechers, D., Cox, P., et al. 2009, Nature, 457, 699
Walter, F., Decarli, R., Aravena, M., et al. 2016, ApJ, 833, 67
Wang, R., Carilli, C. L., Neri, R., et al. 2010, ApJ, 714, 699
Wang, R., Wagg, J., Carilli, C. L., et al. 2013, ApJ, 773, 44
Wang, R., Wu, X.-B., Neri, R., et al. 2016, ApJ, 830, 53
Wang, F., Wang, R., Fan, X., et al. 2019, ApJ, 880, 2
Wang, F., Yang, J., Fan, X., et al. 2021, ApJ, 907, L1
Wang, F., Yang, J., Fan, X., et al. 2024a, ApJ, 968, 9
Wang, W., Wylezalek, D., De Breuck, C., et al. 2024b, A&A, 683, A169
Wenzl, L., Schindler, J.-T., Fan, X., et al. 2021, AJ, 162, 72
Willott, C. J., Omont, A., & Bergeron, J. 2013, ApJ, 770, 13
Willott, C. J., Bergeron, J., & Omont, A. 2015, ApJ, 801, 123
Willott, C. J., Bergeron, J., & Omont, A. 2017, ApJ, 850, 108
Wright, E. L., Eisenhardt, P. R. M., Mainzer, A. K., et al. 2010, AJ, 140, 1868
Wylezalek, D., Galametz, A., Stern, D., et al. 2013, ApJ, 769, 79
Wylezalek, D., Vayner, A., Rupke, D. S. N., et al. 2022, ApJ, 940, L7
Xu, F., Bian, F., Shen, Y., et al. 2018, MNRAS, 480, 345
Yang, J., Wang, F., Fan, X., et al. 2019a, AJ, 157, 236
Yang, J., Venemans, B., Wang, F., et al. 2019b, ApJ, 880, 153
Yang, J., Wang, F., Fan, X., et al. 2020, ApJ, 897, L14
Yang, J., Wang, F., Fan, X., et al. 2021, ApJ, 923, 262
Yang, J., Fan, X., Gupta, A., et al. 2023, ApJS, 269, 27
Yi, W.-M., Wang, F., Wu, X.-B., et al. 2014, ApJ, 795, L29
Yue, M., Eilers, A.-C., Simcoe, R. A., et al. 2024, ApJ, 966, 176
Zanella, A., Daddi, E., Magdis, G., et al. 2018, MNRAS, 481, 1976
Zeimann, G. R., White, R. L., Becker, R. H., et al. 2011, ApJ, 736, 57
Zheng, W., Overzier, R. A., Bouwens, R. J., et al. 2006, ApJ, 640, 574
Zhong, Y., Inoue, A. K., Sugahara, Y., et al. 2024, MNRAS, 529, 4531

Appendix A: Velocity maps

We report here the continuum-subtracted [C II] velocity maps of the RL quasars (see Fig. A.1). We obtained these maps using the CASA task *immoments* with moments=1. We observe different kinematics: the majority of the quasars seem to be characterized by a uniform velocity fields, some with low velocities (e.g., PSO135+16, PSO352-15), another with velocities around ~ -200 km s^{-1} (J1034+2033) and finally PSO055-00 characterized by very high velocities, up to ~800 km s^{-1}. On the other hand, J0131-0321 seem to present more complex features, with a potential disk-like structure, with velocities between +400/−250 km $^{-1}$, and an elongated morphology. However, due to the low spatial resolution and limited S/N, more robust conclusions on the kinematical structure of our sources cannot be drawn. Furthermore, higher resolution and SNR observations are necessary to firmly pin-point the velocity structures of high−z RL quasars.

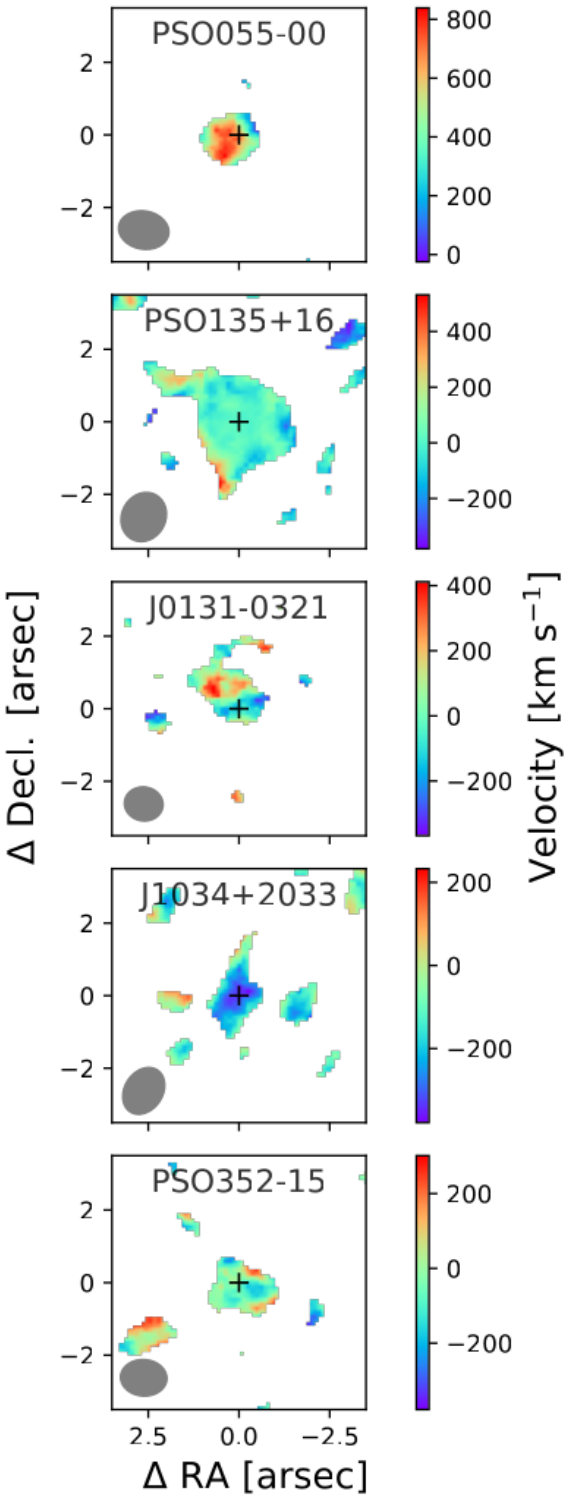

Fig. A.1. ALMA continuum-subtracted [C II] velocity fields.